chemosensors

MDPI

Perspective

Towards Reconstructable CF-LIBS Quantification: A Perspective on Reporting, Validation, and Reproducibility

Homa Saeidfirozeh [1,*], Petr Kubelík [1], Jan Suchánek [1], Jakub Buday [2,3], Pavel Pořízka [2,3], Jozef Kaiser [2,3] and Martin Ferus [1]

[1] Heyrovský Institute of the Czech Academy of Sciences, Dolejškova 3, 182 00 Prague, Czech Republic
[2] Central European Institute of Technology, Brno University of Technology, Purkyňova 656/123, 612 00 Brno, Czech Republic; pavel.porizka@ceitec.vutbr.cz (P.P.)
[3] Institute of Physical Engineering, Faculty of Mechanical Engineering, Brno University of Technology, Technická 2, 616 69 Brno, Czech Republic
* Correspondence: homa.saeidfirouzeh@jh-inst.cas.cz

Abstract

Calibration free laser induced breakdown spectroscopy (CF-LIBS) estimates elemental composition using a plasma model, offering a practical approach where suitable reference standards are unavailable. This Perspective proposes reconstructability as a reporting objective, distinct from physical validity and fitness for purpose. Five checkpoints organize the calculation, illustrated through constructed examples and selected calculations from three published records. The constructed generator and reconstruction share a model; their agreement tests the reporting record, not physical validity. Under the specified ternary-system and uncertainty assumptions, six of nine convention slips move the light minor constituent outside its propagated 95% interval, and three indicators flag seven of nine slips. These counts are case specific. The two undetected linewidth slips are examined in 43 gated xenon–hydrogen spectra using hydrogen lines as a separate density diagnostic. For two bins with median instrumental-to-observed width ratios of 0.50 and 0.58, retaining the instrumental width gives densities 36–61% above the hydrogen-derived estimates and quadrature subtraction by 16–33%, consistent with the calculated effect. Four pulse-energy cases for one regolith simulant demonstrate reconstruction from measured spectra and comparison with X-ray fluorescence (XRF) on a common elemental mass-ratio basis. We distinguish core from recommended reporting items and supply a copyable template. Three analysts recover specified outputs using the supplied code; broader usability and interlaboratory performance remain to be evaluated.

Keywords: calibration free LIBS; laser induced plasma; quantitative analysis; plasma diagnostics; mole and mass fractions; measurement uncertainty; reproducibility; reporting guidelines

Check for updates

Received: 7 October 2026
Revised: 13 November 2026
Accepted: 20 November 2026
Published: 21 November 2026

Copyright: © 2026 by the authors. Licensee MDPI, Basel, Switzerland. This article is an open access article distributed under the terms and conditions of the Creative Commons Attribution (CC BY) license.

1. Introduction

Laser induced breakdown spectroscopy (LIBS) enables rapid analysis of several elements using a focused laser pulse. A small amount of material is ablated, the resulting plasma emits atomic and ionic lines, and a spectrum is recorded within seconds, usually with little or no sample preparation [1–3]. These features have supported the use of LIBS in industrial analysis, handheld analyzers, and planetary rovers [3–5]. However, converting a spectrum into elemental concentrations remains challenging. Line intensities depend on the sample matrix, the interaction between the laser and the sample, and plasma

conditions that vary from pulse to pulse. Quantification therefore commonly relies on suitable standards with a matching matrix, or on multivariate models trained using such standards. Signal uncertainty remains a major obstacle to quantitative performance [1,6–10]. Suitable standards are often unavailable for unknown or unique samples, remote or hazardous environments, and other planetary bodies, where a portable analytical sensor is particularly useful.

Calibration free LIBS (CF-LIBS) was introduced to reduce this dependence on reference standards [11]. Instead of calibrating line intensity against concentration, the method describes emission through a plasma model. The plasma is assumed to represent the sample composition, to be in local thermodynamic equilibrium (LTE), and to be optically thin for the selected lines. Boltzmann and Saha relations connect the measured intensities with the number densities of emitting species, while a closure condition removes the unknown experimental factor [11,12]. Over more than 25 years, developments have included corrections for self absorption [13–15], formulations based on columnar density and $C\sigma$ [16–18], calibration using one point [19–21], spectral simulation [22,23], and automated processing of large spectral datasets [24]. A critical review of departures from nominal compositions found better accuracy for metallic alloys than for dielectrics [12]. An experimental evaluation of alloys and soils obtained the best accuracy for the matrix element and considered the remaining constituents to be determined at a semiquantitative level [25]. Subsequent reviews describe both the progress achieved and the limitations that remain [22,26,27].

These developments also increase the importance of understanding how a reported concentration was obtained. A CF-LIBS calculation involves several connected steps. First, the linewidth is decomposed and used to estimate electron density. Next, line intensities and atomic data provide the temperature, and equilibrium and optical thinness are assessed. Species densities are then summed, normalized, and compared with a reference composition. Each step includes conventions that are not apparent in the final concentration table, such as a half width or a full width, a reference density of 10^{16} or 10^{17} cm^{-3}, intensities in photon or energy units, and mole or mass fractions. Error analyses of the idealized method [28] and of self absorption [29] show how strongly the result depends on the quality of the spectral and atomic inputs. Two recent technical notes examine the physical units used in a Boltzmann plot [30] and the distinction between mole and mass fractions [31]. The latter estimates relative errors ranging from approximately one percent to several hundred percent.

Other measurement communities have addressed similar challenges by agreeing on the information that a publication should provide. The geochronology community using laser ablation inductively coupled plasma mass spectrometry (LA-ICP-MS) adopted shared standards for uncertainty propagation and data reporting [32]. Studies in X-ray photoelectron spectroscopy quantified the occurrence of erroneous peak fitting and insufficient metadata in the literature [33,34]. Quantitative polymerase chain reaction (PCR) has guidelines specifying the minimum information to report [35]. The International Union of Pure and Applied Chemistry (IUPAC) is also defining how spectroscopic data should be made findable and reusable [36,37], following the FAIR principles of findability, accessibility, interoperability, and reusability [38]. Within LIBS, existing resources include recommendations for good practice [6], interlaboratory comparisons [39], open benchmark datasets and contests [40,41], and tutorials on statistical practice [42]. The contribution proposed here is an operational reporting structure rather than a new plasma model or validation criterion. Existing LIBS good-practice recommendations address analytical methodology, figures of merit, and presentation of results [6]; CF-LIBS reviews and technical notes already discuss model assumptions, intensity units, and concentration

basis [12,30,31]. We build on that work by mapping each reported output to five calculation checkpoints, distinguishing four reconstruction outcomes, and connecting numerical inputs, conventions, precision, and executable relationships in one record. The proposed core and recommended tiers make this record usable at a stated calculation boundary. Its general sufficiency for independent users remains to be evaluated.

To address this challenge, we propose that the *reconstructability* of a CF-LIBS calculation should become an explicit reporting objective. A reader should be able to recover the reported numbers from the stated inputs, equations, conventions, and numerical precision. Successful reconstruction does not establish that the physical model is correct. It does, however, make the calculation accessible for examination and helps explain the meaning of agreement with a reference. The paper is organized as follows. Section 2 distinguishes reconstructability from physical validity and fitness for purpose. Section 3 introduces five checkpoints along the quantification chain and identifies the choices that may remain implicit at each stage. Section 4 summarizes reporting patterns encountered during reconstruction attempts, illustrates them with three published records, and uses a constructed record to compare individual convention errors with plausible input uncertainties. It also examines whether these errors could be recognized without access to the record. Section 5 proposes a minimum reporting record connected with executable calculations and discusses its limitations. Section 6 presents an agenda for evaluation and adoption.

The scope of this Perspective has two boundaries. First, it is a personal assessment informed by our attempts to reconstruct a small number of published CF-LIBS calculations for several material classes and by our work on LIBS for space applications [5]. It is not a systematic survey and does not estimate the frequency of the reporting patterns. Second, this Perspective discusses reporting patterns at the level of calculation steps. Three published records illustrate these patterns without establishing the quality of the underlying measurements. Constructed examples are identified as such and supplied in Supplementary Text S1 and Code S1. The published records are documented separately in Supplementary Text S2. Supplementary Text S3 applies the same calculation to measured spectra of one regolith simulant at four pulse energies. These cases examine implementation and dependence on acquisition conditions under declared assumptions; they do not establish general experimental validity.

2. Three Questions Behind One Number

2.1. The Calculation in Brief

In its basic formulation [11,12], CF-LIBS describes the intensity integrated over wavelength for a transition from an upper level k to a lower level i of element s in charge state z as

$$I_{ki} = F n_{s,z} \frac{g_k A_{ki}}{U_{s,z}(T)} \exp\left(-\frac{E_k}{k_B T}\right), \quad (1)$$

where $n_{s,z}$ is the number density of the emitting species, g_k and E_k are the statistical weight and energy of the upper level, A_{ki} is the transition probability, $U_{s,z}(T)$ is the partition function, T is the temperature, k_B is the Boltzmann constant, and F is an experimental factor common to all lines. Equation (1) applies to intensities proportional to the number of photons. For intensities expressed in energy units, the right hand side is multiplied by hc/λ_{ki}, where h is the Planck constant, c is the speed of light, and λ_{ki} is the transition wavelength. The Boltzmann plot is obtained by plotting $\ln[I_{ki}/(g_k A_{ki})]$ against E_k. Its slope, $-1/(k_B T)$, gives the temperature, while its intercept, $\ln[F n_{s,z}/U_{s,z}(T)]$, contains the

species density and the common factor F. The densities of successive charge states are connected through the Saha equation,

$$N_e \frac{n_{s,II}}{n_{s,I}} = 2\frac{U_{s,II}(T)}{U_{s,I}(T)}\left(\frac{2\pi m_e k_B T}{h^2}\right)^{3/2} \exp\left(-\frac{E_{ion}}{k_B T}\right), \quad (2)$$

where N_e is the electron density, I and II denote neutral and singly ionized species, m_e is the electron mass, and E_{ion} is the ionization energy of the neutral atom of element s, reduced where relevant by its lowering in the plasma. Finally, summing over charge states and normalizing over the included elements gives

$$x_s = \frac{\sum_z n_{s,z}}{\sum_j \sum_z n_{j,z}}, \qquad \sum_s x_s = 1, \quad (3)$$

which eliminates F. The quantities x_s are number fractions, or mole fractions, over the set of elements included in the denominator.

2.2. Reconstructability, Physical Validity, and Fitness for Purpose

Figure 1 shows the sequence of operations from a spectrum to a composition and its validation. At each stage, it identifies choices that affect the result but are not visible in a concentration table. Three questions are useful when assessing such a table. First, is the result reconstructable: do the stated inputs, equations, and conventions recover the reported numbers? Second, is it physically supported: is there evidence that the plasma model assumptions hold for the selected lines? Third, is it fit for purpose: does it agree with independent information within a stated uncertainty that meets the analytical requirement?

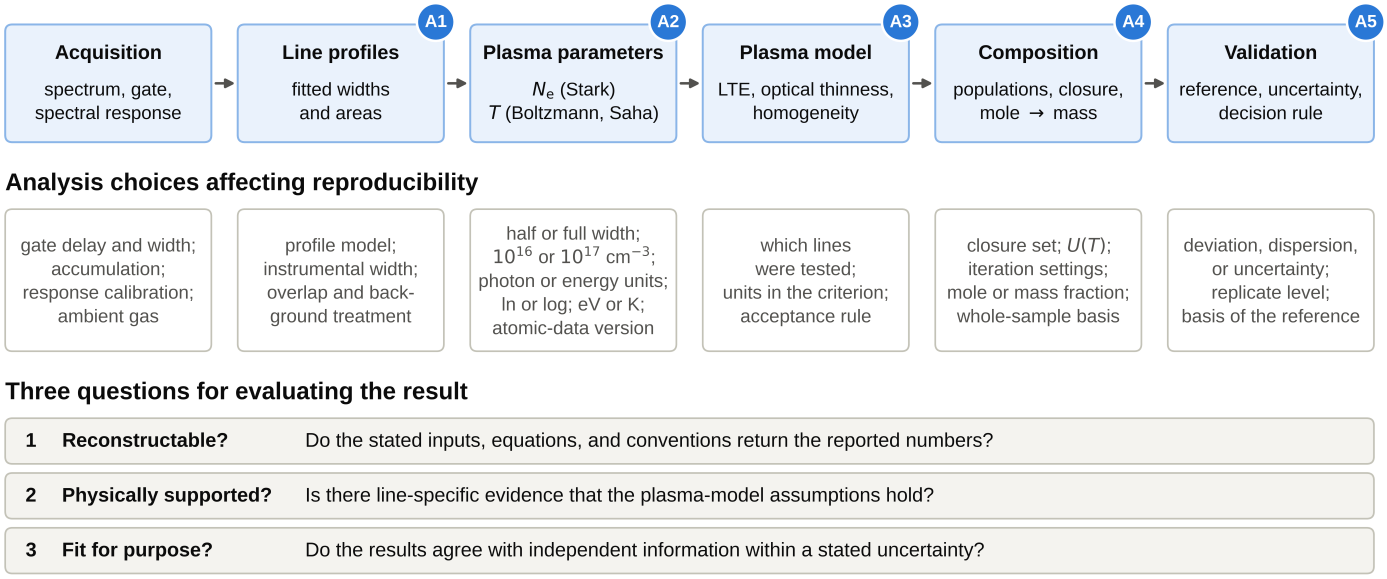


Figure 1. The CF-LIBS quantification chain and the five reporting checkpoints, A1 to A5, proposed in this Perspective. The middle row gives examples of choices that affect the result or its interpretation without appearing in the final concentration table. Acquisition conditions provide context for every checkpoint. The bottom rows state the three questions distinguished in Section 2.

A positive answer to one question does not answer the other two. A Stark density calculation may be fully reconstructable even when the adopted width includes the instrumental profile. Conversely, a sound experiment may lack sufficient documentation to recover its numerical results. Close agreement with a reference does not establish that the intermediate steps are reconstructable or that the comparison uses the same

concentration basis. The three questions also depend on one another to different degrees. Fitness for purpose can, in principle, be established empirically through validation against independent reference materials without access to the calculation. This is how an analyzer with an inaccessible calculation can be qualified. Such validation applies to the matrices and conditions examined. CF-LIBS is often used where suitable reference materials are unavailable, so the calculation itself must then provide the evidence and remain open to inspection.

Computational reconstructability means recovering a stated numerical output from fixed recorded inputs and a specified calculation, within a declared tolerance. It corresponds to reproducibility in computational research [43]. Experimental repeatability and reproducibility instead concern new measurements under the same or specified changed conditions [44,45]. Analytical reliability concerns evidence about bias, precision, uncertainty and robustness for a defined measurand and application. The five 20-shot groups used at each energy in Section 4.4 describe within-acquisition variation, not interlaboratory reproducibility or total uncertainty. Preserving existing inputs can improve reconstructability; recovering a missing instrumental profile or reference uncertainty may require additional measurements.

2.3. Four Outcomes of a Reconstruction Attempt

A calculation step can lead to four reconstruction outcomes. A step is *reconstructed* when the reported value falls within the interval obtained by propagating the printed precision of the stated inputs. It is *internally inconsistent* when those inputs and relations do not recover the accompanying value. A *reporting gap* occurs when a required input or convention is missing or ambiguous, preventing confirmation or rejection of the step. Finally, a *conditional result* holds only under an assumption that is not established by the record. These descriptions apply to calculation steps and require different responses: no change, a correction, a clarification, or additional data. They are used in Section 4 and do not assign an overall judgment to a study or its authors.

A value printed to an increment d represents a rounding interval with half width $d/2$. This interval describes the numerical representation and is distinct from measurement uncertainty. Nevertheless, it limits what can be reconstructed. When an equation containing a small coefficient is inverted, rounding of that coefficient can dominate the result, as discussed in Section 3.4. Coefficients and intermediate quantities should therefore be archived at full working precision even when fewer digits are displayed in the article.

3. Five Checkpoints Along the Quantification Chain

Table 1 presents the five checkpoints, A1 to A5, in the order of the calculation, from spectral observables to analytical validation. They specify what must be recoverable while allowing different approaches to the analysis. A classical intercept calculation, an iterative method using Saha–Boltzmann plots [46], a formulation corrected for self absorption, and an approach based on spectral simulation answer the same questions using different equations. Several operations precede all five checkpoints. Before a line enters the calculation, the continuum has been subtracted, integration limits have been defined, overlapping lines have been separated, and lines have been selected or rejected. These operations determine the intensities and widths used throughout the analysis. We therefore include them in the context required by every checkpoint, as discussed in Section 5.

Table 1. The five checkpoints for reconstructable CF-LIBS quantification. Each question concerns an identifiable part of the reported calculation and does not provide a verdict on the study as a whole.

Stage	Focus	Question That the Published Record Should Answer
A1	Linewidth provenance	Which observed and fitted profile components enter the electron density estimate, and how are the instrumental and other contributions treated?
A2	Plasma parameters	Do the stated equations, units, constants, atomic data, and broadening conventions return the reported temperature and electron density?
A3	Plasma model evidence	What numerical evidence for specific lines supports LTE, optical thinness, and the other assumptions, and to which lines and acquisition window does it apply?
A4	Concentration calculation	Can the calculation of the species densities be executed with the stated closure set, partition functions, charge states, and iteration settings, and on which basis (mole or mass; subset or whole sample) are the results expressed?
A5	Validation	Are reference values, concentration bases, replicate definitions, uncertainty components, and agreement criteria stated so that deviation, dispersion, and uncertainty can be told apart?

3.1. A1: Linewidth Provenance

Electron density is most often obtained from Stark broadening of an isolated line [46,47]. For a line of a nonhydrogenic species broadened predominantly by electron impact, the relation is

$$N_e = \frac{\Delta\lambda_S}{2\omega} N_{ref}, \tag{4}$$

where $\Delta\lambda_S$ is the Stark full width at half maximum (FWHM) and ω is the Stark parameter, here defined as the electron impact half width at half maximum (HWHM) tabulated at reference density N_{ref}. A correction for ion broadening, usually small under LIBS conditions, is omitted [46,47]. The first checkpoint concerns the numerator: the width used in Equation (4) must be the Stark component of the observed width. The observed profile is a convolution of the Lorentzian Stark profile with the instrumental and Doppler profiles, and self absorption may broaden it further [15,46]. For a Lorentzian profile of FWHM $\Delta\lambda_S$ convolved with a Gaussian profile of FWHM G, the resulting Voigt profile has an FWHM W given by the following approximation [48]:

$$W \simeq 0.5346\,\Delta\lambda_S + \sqrt{0.2166\,\Delta\lambda_S^2 + G^2}. \tag{5}$$

The familiar quadrature rule, $\Delta\lambda_S = \sqrt{W^2 - G^2}$, is exact only when both profiles are Gaussian. Applying it to a Lorentzian line removes too little instrumental broadening. Figure 2 illustrates the consequence, with numerical values provided in Table S1. When the instrumental width is 40% of the observed width, neglecting it overestimates N_e by approximately 20%, while quadrature subtraction still gives an overestimate of approximately 10%. At 80%, the corresponding overestimates are approximately 190% and 74%. These calculations assume a Gaussian instrumental profile. If the instrumental profile is instead close to a Lorentzian, the widths add linearly, and the overestimates at 40% increase to 67% and 53%. The profile shape is therefore required together with its width. As the observed width approaches the instrumental width, the Stark component becomes poorly determined even when the fitted profile appears satisfactory. The instrumental width should be measured at, or interpolated to, the diagnostic wavelength. A nominal resolving power does not replace this information.

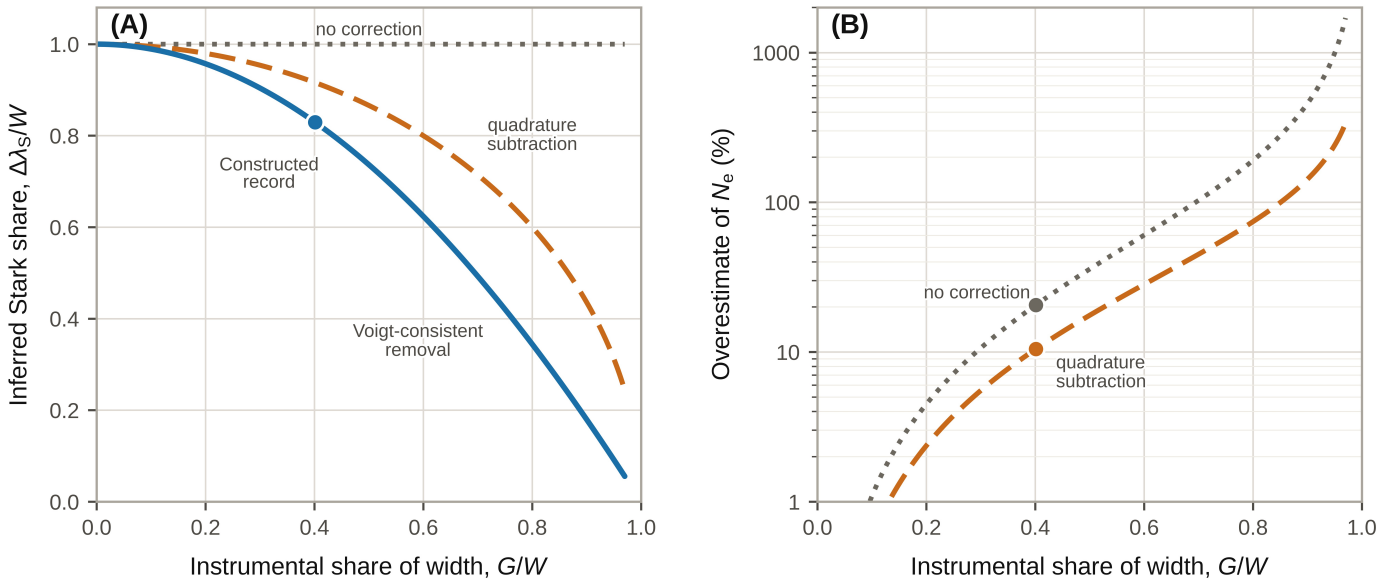


Figure 2. Effect of the instrumental profile on electron density calculated from a Stark width. The Lorentzian line is observed with a Gaussian instrumental profile of full width at half maximum G, and W is the observed width. (**A**) Fraction of the observed width attributed to Stark broadening when the instrumental contribution is neglected, subtracted in quadrature, or removed consistently with a Voigt profile using Equation (5). (**B**) Resulting overestimate of electron density relative to the value consistent with the Voigt profile. The circles indicate the constructed record of Section 4.2, for which $G/W = 0.40$. All values are calculated and do not represent measurements.

3.2. A2: Plasma Parameters, Atomic Data, and the Intensity Scale

The second checkpoint asks whether the stated equations, data, and conventions recover the reported electron density and temperature. Equation (4) contains two conventions that require particular attention. Griem's semiclassical tables give half widths referred to 10^{16} cm^{-3} for neutral emitters and 10^{17} cm^{-3} for singly ionized emitters [47]. Critical compilations and databases instead give full widths at the densities used in the original experiments or calculations [49,50]. Confusing half and full widths changes N_e by a factor of 2, while confusing the two reference densities changes it by a factor of 10. The latter exceeds plausible measurement uncertainty. A factor of 2 can be less apparent because critically evaluated Stark widths have estimated uncertainties from approximately 15% to more than 50%, depending on the line [49]. Neither convention can be recovered from a table containing only the final electron density. The record should therefore provide the Stark parameter, its source and definition, the reference density and temperature, and the uncertainty propagated through the calculation. For a hydrogen Balmer line, the tabulation used to convert the measured width into density provides the corresponding information [51].

The ordinate of the Boltzmann plot introduces similar choices. With intensities in energy units, the logarithm includes a factor λ_{ki}; with intensities in photon units, it does not. Replacing a natural logarithm with a decadic logarithm changes the slope by a factor of 2.303. Energies of upper levels may be expressed in eV or cm^{-1}, and temperatures in K or eV, with 1 eV corresponding to 11,604.5 K. The same care is needed for the Saha equation. The prefactor of Equation (2), $2(2\pi m_e k_B/h^2)^{3/2}$, is 4.83×10^{15} cm^{-3} K$^{-3/2}$ when temperature is expressed in K and 6.04×10^{21} cm^{-3} eV$^{-3/2}$ when expressed in eV. A technical note emphasizes that the logarithm must have a dimensionless argument formed from radiometrically calibrated intensities. In its example using two lines, an uncorrected spectral response that varied with wavelength changed a temperature of 10,000 K into 7444 K [30].

These choices matter because composition depends exponentially on temperature. The Boltzmann contribution to the species density inferred from a line with upper level energy E_k scales as $\exp[E_k/(k_B T)]$. Its logarithmic sensitivity to temperature is therefore $-E_k/(k_B T)$, ranging from approximately -3.5 to -7 for energies between 3 and 6 eV at 10,000 K. The Saha ratio has a still greater sensitivity, $3/2 + E_{ion}/(k_B T)$, or approximately 8.5 to 12 for ionization energies between 6 and 9 eV. A temperature 5% too high increases the calculated ratio of ions to neutral atoms by a factor of 1.5 to 1.8. Two effects moderate these sensitivities in practice. Partition functions increase with temperature and partly offset the Boltzmann contribution. In a normalized composition, a factor common to all species cancels, leaving the differences between species and the charge states supplied by the Saha equation. The temperature also inherits the relative uncertainty of the fitted slope, which depends on the range of upper level energies and scatter of the fitted points. Transition probabilities contribute directly to this scatter. Their accuracy classes in the Atomic Spectra Database of the National Institute of Standards and Technology (NIST) range from AAA ($\leq$0.3%) to E (>50%) [52].

Section 5 lists the information needed to recover the temperature, including the actual line list, intensity definition, and physical constants [53]. When electron density is obtained from both Stark broadening and a Saha balance, both values should be retained. Their agreement provides one of the few internal consistency checks available to the method, as discussed in Section 4.3.

3.3. A3: Evidence for the Plasma Model

CF-LIBS assumes stoichiometric ablation, LTE, optical thinness of the analytical lines, and a plasma sufficiently homogeneous to be described by one temperature and one electron density [12,22,54]. The evidence for each assumption should be reported together with the lines to which it applies. For LTE, the usual diagnostic is the McWhirter criterion [55],

$$N_e(\mathrm{cm}^{-3}) \geq 1.6 \times 10^{12} [T(\mathrm{K})]^{1/2} [\Delta E(\mathrm{eV})]^3, \quad (6)$$

where ΔE is the largest energy gap between adjacent levels. This is a necessary condition derived for a stationary and homogeneous plasma. In a transient, expanding plasma produced by a laser, the relaxation time of excited state populations must also be short relative to the time over which T and N_e change. The distance over which atoms diffuse during this relaxation time must be small relative to the lengths over which plasma gradients occur [56]. Reporting the inputs is also necessary because the threshold depends on their units. For $T = 10{,}000$ K and $\Delta E = 3.14$ eV, the threshold is $4.95 \times 10^{15}\,\mathrm{cm}^{-3}$. Substituting the temperature as 0.8617, its numerical value in eV, gives $4.60 \times 10^{13}\,\mathrm{cm}^{-3}$, lower by a factor of approximately 107.7. In a dense plasma, the diagnostic conclusion may remain unchanged despite this error. At late delays or low pressures, however, the conclusion itself can change, and the printed threshold cannot be recovered from the correctly stated inputs.

Optical thinness is commonly examined by comparing the measured intensity ratio of two lines of the same species with the ratio expected from their atomic parameters. This test applies to the selected lines and the assumed temperature. Resonance lines of major elements are the first to be affected by self absorption and are not covered unless they were tested or excluded [15,29]. When a correction for self absorption is applied, the coefficient for each line becomes an input that should be retained. In our experience, evidence for homogeneity is supplied less often than for the other assumptions, although recent $C\sigma$ procedures explicitly account for plasma inhomogeneity [18]. Evidence for stoichiometric ablation usually comes from outside the emission spectrum, through the irradiance regime and knowledge of material fractionation [1,12]. Its source can be stated in the record.

Acquisition conditions provide context for all checkpoints and are particularly relevant here. Gate delay and width determine whether emission is collected from a plasma close to equilibrium or integrated over its evolution. Many compact and handheld instruments use detectors without time gating [4], so they average over a range of temperatures and densities. Any measurement along a line of sight also averages over space. Each study need not apply every available diagnostic, but the claimed domain of validity should match the evidence provided. The record should distinguish an inapplicable item, an examined item, and an item that was not assessed.

3.4. A4: From Populations to Reported Concentrations

Species densities are converted into a reported composition through three steps. Each step can change the final result while leaving all spectral quantities unchanged.

The closure set. Equation (3) normalizes the populations over the included elements. Unobserved charge states must be supplied through Equation (2), which requires N_e, T, both partition functions, and the ionization energy. Partition functions depend on temperature and on the levels included in their sums; they cannot be replaced by the statistical weight of the ground level. Ionization energy is lowered in the plasma. For $N_e = 10^{17}$ cm^{-3} and 10,000 K, an estimate using the Debye–Hückel model gives 0.07 to 0.09 eV, increasing the Saha ratio by approximately 10% (Supplementary Text S1). The record should therefore state whether this lowering was included. Iterative methods additionally require starting values, update rules, tolerances, and a termination criterion. Convergence shows that the iteration stopped without establishing that the solution is unique. Elements without a usable line in the measured range, often O, N, H, C, or the halogens, are either excluded or assigned through stoichiometry, for example as oxides. The normalized composition then refers to that selected set and to the adopted stoichiometric assumption.

The concentration basis: Equation (3) gives mole fractions, while reference compositions are almost always expressed as mass fractions w_s. The two are related by

$$w_s = \frac{x_s M_s}{\sum_j x_j M_j}, \qquad x_s = \frac{w_s / M_s}{\sum_j w_j / M_j}, \tag{7}$$

where M_s is the molar mass of element s. A recent technical note points out that this conversion is rarely described in CF-LIBS publications. Omitting it produces errors that increase with the difference between M_s and the mean molar mass of the sample [31]. Equation (7) gives $x_s/w_s = \bar{M}/M_s$, with $\bar{M} = \sum_j x_j M_j$. Every element in every sample therefore follows the same curve in Figure 3. Table 2 illustrates familiar examples. Aluminum at 6% by mass in a Ti alloy containing 6% Al and 4% V corresponds to 10.2% by mole, while nickel at 7% by mass in a tungsten heavy alloy corresponds to 18% by mole. Both composition vectors sum to unity, so normalization alone cannot identify the basis of the reported values.

The sample basis: Mass fractions over the closure set represent the whole sample only when that set includes all major constituents. This is not the case for an organic or hydrated matrix. In a constructed example of dried biological material, the detected mineral elements account for 4.2% of the dry mass. Normalization over those elements gives 48% for an element actually present at 2.0% of the dry mass (Supplementary Text S1). Expressing the result in mg kg^{-1} of the sample requires an independent anchor. This may be a constituent with a known concentration, an independently measured ash or mineral fraction, or inclusion of the matrix elements in the closure set. Results based on dry mass, wet mass, ash, or oxides describe different quantities, and each basis should be stated separately.

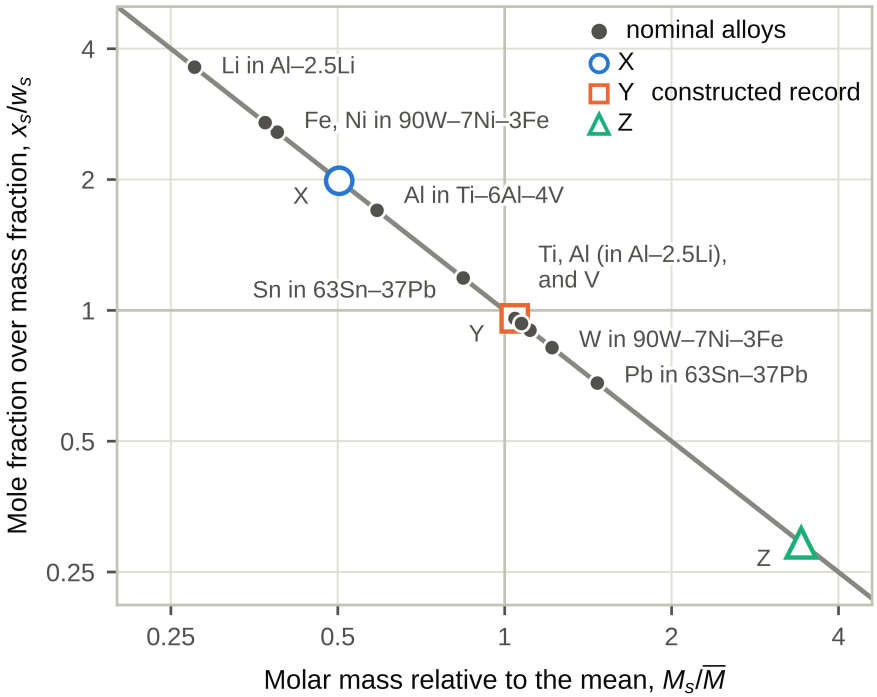


Figure 3. Ratio of mole fraction to mass fraction as a function of an element's molar mass relative to the mean molar mass of the sample. The line follows $x_s/w_s = \bar{M}/M_s$ from Equation (7). Symbols show selected examples from Table 2. Filled circles represent nominal alloy compositions. The open circle, square, and triangle represent X, Y, and Z in the constructed record, respectively. The ordinate also gives the factor by which a mass fraction is misstated when a mole fraction is reported in its place.

Table 2. Mass and mole fractions for the nominal compositions of four familiar alloys, the Cu–Fe alloy of Case B (Section 4) and the hypothetical sample used in the constructed record of Section 4.2. Molar masses of real elements are abridged standard atomic weights [57]. The nominal compositions illustrate basis conversion; measured values for the Cu–Fe alloy are compared in Section 4.5.

Material	Element	M_s (g mol^{-1})	Mass Fraction (%)	Mole Fraction (%)	x_s/w_s
Ti alloy: 6% Al, 4% V	Ti	47.867	90.00	86.20	0.96
	Al	26.982	6.00	10.20	1.70
	V	50.942	4.00	3.60	0.90
90% W, 7% Ni, 3% Fe	W	183.84	90.00	73.89	0.82
	Ni	58.693	7.00	18.00	2.57
	Fe	55.845	3.00	8.11	2.70
63% Sn, 37% Pb	Sn	118.71	63.00	74.82	1.19
	Pb	207.2	37.00	25.18	0.68
Al alloy: 2.5% Li	Al	26.982	97.50	90.93	0.93
	Li	6.94	2.50	9.07	3.63
Cu–Fe alloy: 20% Cu	Cu	63.546	20.00	18.01	0.90
	Fe	55.845	80.00	81.99	1.02
Constructed record (hypothetical elements)	X	27.0	6.00	11.92	1.99
	Y	56.0	91.00	87.20	0.96
	Z	184.0	3.00	0.87	0.29

A further situation arises when a workflow described as calibration free includes an empirical relation fitted to reference samples and inverted to obtain concentrations in new samples. Such a step uses calibration information and produces a calibrated result. It also inherits the sensitivity of inverse regression when the slope is small. For a linear relation

$y = a + bC$ between a measured quantity y and concentration C, with fixed coefficients a and b, the relative uncertainty contributed by y is multiplied by $|(a + bC)/(bC)|$ in the recovered concentration. In a constructed case, this factor is 10: a 5% uncertainty in y becomes a 50% uncertainty in concentration. Printing the slope with one significant digit changes the recovered C by -9% to $+11\%$ (Supplementary Text S1).

3.5. A5: Validation and Measurement Uncertainty

When a CF-LIBS result C_m is compared with a reference value C_r, deviation, dispersion, and uncertainty address different questions. The signed relative deviation,

$$\delta = 100\frac{C_m - C_r}{C_r}, \tag{8}$$

compares the central values. The relative standard deviation, RSD $= 100 s_C/\bar{C}$, describes the dispersion of a defined set of replicates with mean $\bar{C}$ and standard deviation s_C. Measurement uncertainty combines all contributions, including those that remain unchanged between replicates [58–60]. Compatibility with a reference can then be assessed through the normalized deviation used in proficiency testing [61],

$$\zeta = \frac{C_m - C_r}{\sqrt{u_m^2 + u_r^2}}, \tag{9}$$

where u_m and u_r are the standard uncertainties of the two values, assumed to be uncorrelated. The condition $|\zeta| \leq 2$ is conventionally taken to indicate compatibility.

In a constructed comparison, five replicates have a mean of 47.9 and a standard deviation of 0.60, corresponding to an RSD of 1.3%. They are compared with a reference value of 45.0 with a standard uncertainty of 0.30. The relative deviation is $\delta = +6.4\%$. Describing this result as agreement "within 1.3%" would confuse dispersion with deviation. Whether the 6.4% deviation is acceptable depends on the uncertainty model. Taking the standard deviation of the mean, $0.60/\sqrt{5} = 0.27$, as the only method uncertainty gives $\zeta = 7.2$. Taking a relative standard uncertainty of 6% of the result, or 2.87, gives $\zeta = 1.0$. The interpretation therefore depends on an uncertainty budget that cannot be supplied by replicate scatter alone. In our assessment, contributions not sampled by replicates often dominate this budget: the Stark parameter, transition probabilities, partition functions, spectral response calibration, and the model assumptions themselves. A numerical study of the idealized method examined several of these contributions [28]. Section 4.2 provides an example in which a repeatability of 2.9% coexists with a combined standard uncertainty of 26%.

A reference comparison also has its own limitations. Normalization makes the fraction of a dominant element relatively insensitive to calculation errors, as shown in Section 4.2. This is consistent with the observation that the matrix element usually gives the best accuracy [25]; minor constituents carry more information about such errors. The two methods also rarely examine the same amount of material. A laser pulse ablates a mass smaller by orders of magnitude than the portion consumed by a technique using digestion. The reference basis, such as dry mass or oxide composition, must also match the CF-LIBS basis. Finally, repeated pulses at one spot, repeated spots, repeated pellets, and independent materials examine different sources of variation. Agreement for one material cannot establish performance across an entire class of matrices [59,60].

4. Reporting Patterns and Their Consequences

4.1. Patterns Encountered During Reconstruction

Table 3 summarizes methodological reporting patterns informed by our reconstruction experience. The table discusses calculation steps without assigning an overall judgment to a study or its authors. For each pattern, the table identifies the reconstruction outcome introduced in Section 2, the conclusion supported by the available information, and the information needed to resolve it.

Table 3. Reporting patterns in CF-LIBS quantification. Checkpoints refer to Table 1, and outcomes follow Section 2. An individual pattern does not establish that the underlying measurement is incorrect. The three re-analysed records illustrate reporting patterns only; they do not assess the overall quality of the original works.

Stage	Pattern	Outcome	Supported Conclusion	Information Needed
A1	The observed width is used as the Stark width, without the instrumental profile at the diagnostic wavelength.	Reporting gap	Substitution into Equation (4) can be recovered. The density is an upper bound at an unknown distance from the value based on Stark broadening alone.	Instrumental profile at the diagnostic wavelength; fitted Lorentzian and Gaussian components.
A2	The Stark relation, tabulated parameter, and reported density imply different conventions for half or full width, or for 10^{16} or 10^{17} cm^{-3}.	Internal inconsistency	An inconsistency is established only when the stated definitions and inputs conflict. If the definition is absent, the outcome is a reporting gap; a factor of 2 or 10 alone does not identify the cause.	Definition, reference density, and source of the Stark parameter; one worked substitution.
A2	Temperature values or units differ between sections, or the Boltzmann ordinate is undefined.	Internal inconsistency; reporting gap	Conflicting stated values are an internal inconsistency; an undefined ordinate or missing input is a reporting gap. These are recorded separately.	Line list and atomic data as used; ordinate, units, and fit output.
A3	The printed LTE threshold does not follow from the temperature and energy gap, for example because units were mixed.	Internal inconsistency	The correctly evaluated inequality may still hold. The conclusion can remain valid although the printed number does not.	Inputs and units of the criterion.
A3	Optical thinness is tested using lines other than those used for quantification.	Conditional result	The test supports the tested lines. It extends to the analytical lines only if their behavior is comparable.	Analytical lines covered and not covered by the test.
A4	A relation fitted to reference samples is used within a calibration free workflow, with coefficients rounded beyond the precision needed for inversion.	Reporting gap	The concentrations cannot be regenerated, and the step uses calibration information.	Coefficients at full precision; calibration samples; inversion procedure.
A4	Population equations are followed by weight percentages without a conversion step.	Reporting gap	The values cannot be identified as mole or mass fractions. Both bases sum to 100%.	Fractions before and after conversion; molar masses.
A4	Normalization over detected elements is reported in mg kg^{-1} of the sample.	Conditional result	The values describe the detected set unless an anchor to the whole sample is supplied.	Closure set; whole sample anchor; dry, wet, or ash basis.
A5	A dispersion measure is described as agreement with a reference, or its definition is omitted.	Reporting gap	An undefined percentage is a reporting gap. If a percentage explicitly claimed as central-value agreement conflicts with the paired values, that claim is internally inconsistent; uncertainty may still be unknown.	Paired values; signed deviations; replicate structure; uncertainty budget.

Most of these patterns concern information that was already available when the article was prepared. Several can occur in otherwise sound work. For example, evaluating an

LTE criterion with consistent units or recalculating an intensity ratio from the reported line intensities can confirm the original conclusion. A complete reporting record can therefore support sound results as well as identify errors. Apart from the final row of Table 3, the patterns are not apparent from the final concentration table.

The three records were selected because their printed numerical inputs permit direct inspection of different calculation steps in three matrices: reference-deviation arithmetic (Case A, soil), intensity-ratio reconstruction (Case B, alloy), and the connection between normalized populations and absolute concentrations (Case C, plant). They do not form a systematic or representative sample. In Case A [62], the printed Cd values give $\delta = -6.61\%$ and $+8.88\%$: the deviation arithmetic is reconstructed, while the stated approximately $\pm 1\%$ agreement is internally inconsistent with those central values. This does not establish statistical incompatibility without an uncertainty budget. In Case B [63], the central ratio comparisons are reconstructed, while the complete composition calculation has a reporting gap. In Case C [64], the McWhirter substitution is reconstructed; the Stark substitution is conditional on assigning the total fitted width to Stark broadening; instrument-corrected density and absolute concentration closure remain reporting gaps. These labels apply only to the specified steps. Supplementary Text S2 and its provenance table identify source locations, assumptions, substitutions, rounding, and unavailable uncertainty. Source citations are retained so that the cases remain verifiable; no assessment of the authors or overall study quality is implied.

4.2. The Effect of Conventions in a Constructed Record

To examine these choices under controlled conditions, we constructed a complete reporting record for a hypothetical ternary sample (Supplementary Text S1, Table S2, and Data S1). The sample comprises a light minor constituent X at 6% by mass, a major matrix element Y at 91%, and a heavy minor constituent Z at 3%. Their molar masses, ionization energies, partition functions, and line data were assigned values of realistic magnitude. A forward LTE model at $T = 10{,}000$ K and $N_e = 1.00 \times 10^{17}$ cm^{-3} generated 21 line intensities in five replicates with 3% relative Gaussian noise and a diagnostic line broadened according to a Voigt profile. X is observed through neutral lines, Z through ionic lines, and Y through both charge states. The unobserved states of X and Z are calculated using the Saha equation.

The record follows the minimum reporting structure proposed in Section 5. The reader reconstruction script regenerates 18 deterministic reported values within their printed precision and seven values obtained by Monte Carlo propagation using the documented seed (Code S1). The generator and reconstruction script share the same model. This exercise therefore demonstrates reconstruction from the supplied record within a shared idealized model. It does not establish physical validity, experimental composition accuracy, or usability by independent analysts. A separately formulated numerical implementation can check the calculation without validating the shared plasma model. It is a favorable case with assigned atomic data and noise, and no spectral line fitting.

The baseline reconstruction gives $T = 9990$ K, with a standard deviation of 35 K across the five replicates, and $N_e = 1.00 \times 10^{17}$ cm^{-3}. The recovered mass fractions are 5.98%, 91.03%, and 2.98% for X, Y, and Z, respectively (Table S3 and Figure S1). Their replicate RSDs are 2.9%, 0.2%, and 1.5%. Next, we propagated the assigned standard uncertainties of the Stark parameter (20%), transition probabilities (10%), partition functions (5%), and the two widths using a Monte Carlo calculation [65]. The resulting standard uncertainties are 180 K for temperature and 21% for electron density. The combined relative standard uncertainties of the mass fractions are 26%, 1.6%, and 9.4%.

The propagated temperature uncertainty is approximately five times the replicate standard deviation. For X, the combined relative uncertainty is nine times the replicate

RSD. These ratios depend on the assigned uncertainties and noise model. The underlying mechanism is more general. Approximately 90% of X is ionized, while only its neutral lines are observed. Its total density is therefore inferred mainly through the Saha equation, with the sensitivities discussed in Section 3.2. The recovered distribution is skewed, with a 95% interval from 3.7% to 9.8% by mass.

We then introduced 13 individual perturbations (Figure 4 and Table S4). Four represent errors in inputs or plasma parameters and provide a comparison. U1 increases temperature by 5%, corresponding to approximately 2.7 times the propagated standard uncertainty in this example, calculated from the unrounded outputs. That uncertainty budget excludes response calibration, correlated errors in transition probabilities, and model error. U2 increases the Stark parameter by 20%, and U3 increases the transition probabilities of the X I lines by 10%. U4 introduces a spectral response tilt of 5% per 100 nm. Its effect on composition is below 1% for this line list because of partial cancellation.

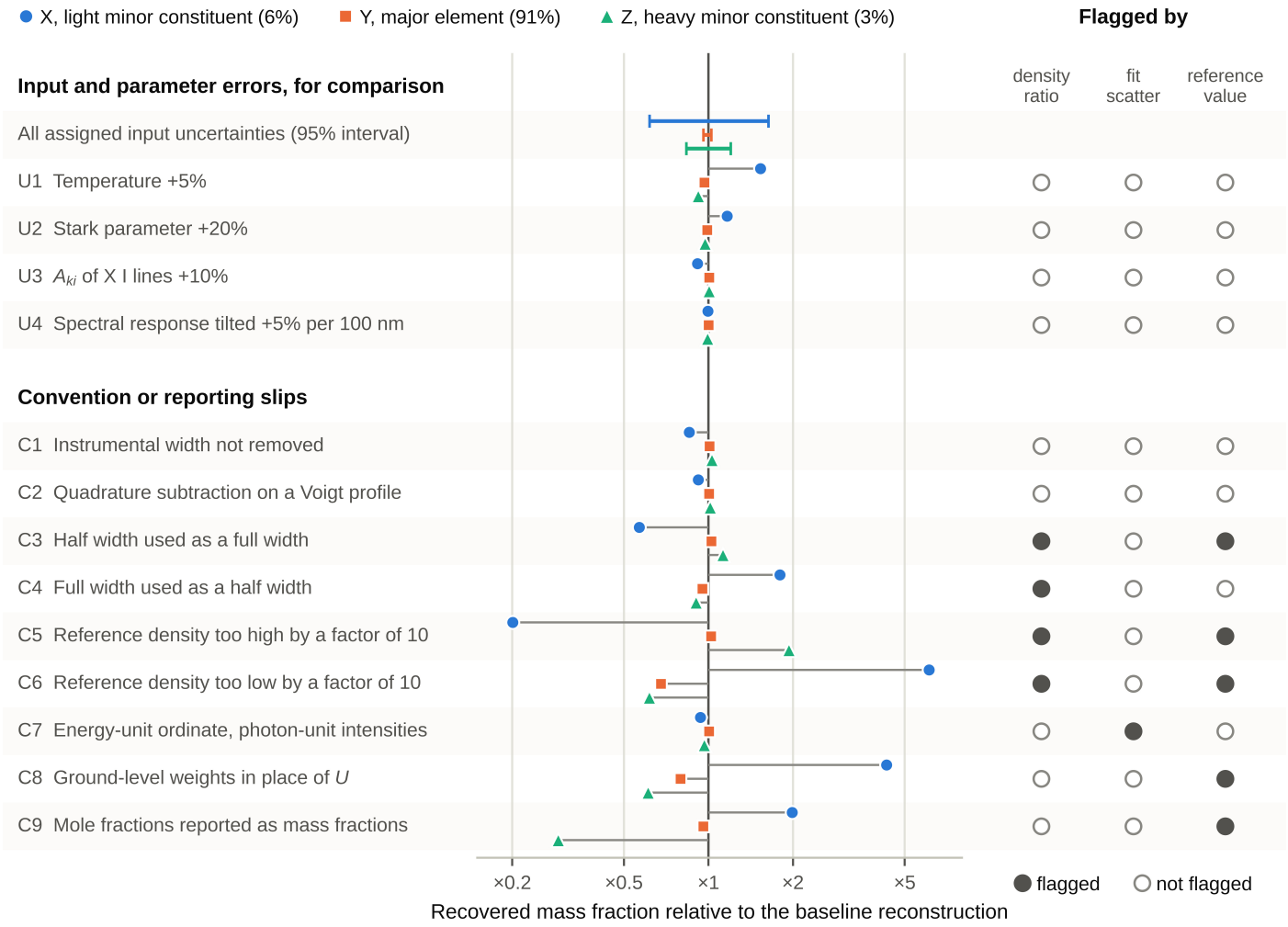


Figure 4. Effect of individual perturbations on the mass fractions recovered from the hypothetical ternary record, relative to the baseline reconstruction, on a logarithmic scale. The upper group shows input and plasma parameter errors together with the 95% interval from Monte Carlo propagation of all assigned input uncertainties. The lower group shows convention or reporting slips. The matrix identifies perturbations flagged by the ratio of electron density from the Saha balance to that from the Stark width, outside its 95% range under input uncertainties; by the residual scatter of the Boltzmann plot, above its corresponding 95% range; or by comparison with the reference, with $|\zeta| > 2$ for at least one element. Every perturbed composition sums to 100%. The magnitudes apply to this constructed case, and the values are listed in Tables S4 and S5.

The remaining nine perturbations, C1 to C9, represent convention or reporting slips discussed in Section 3. The reference density slips change the recovered fraction of X to 0.20 times the baseline in C5 and 6.1 times the baseline in C6. Interpreting a half width as a full width reduces X by 43% in C3; the reverse interpretation increases it by 80% in C4. Substituting statistical weights of the ground levels for partition functions increases X by a factor of 4.3 in C8. Leaving the composition as mole fractions doubles X and reduces Z to less than one third in C9. The other three slips have smaller effects. Retaining the instrumental contribution in the Stark width reduces X by 15% in C1; subtracting it in quadrature reduces X by 8% in C2. Applying an ordinate for energy units to intensities in photon units reduces X by 6% in C7. The effect of C7 depends on the correlation between wavelength and upper level energy in the selected lines. For comparison, U1 increases X by 53%, and U2 increases it by 17%.

Two observations follow from this comparison. First, six slips, C3 to C6, C8, and C9, move X outside the 95% interval obtained from propagated input uncertainties. This interval extends from 0.62 to 1.64 times the baseline fraction, and none of the four comparison perturbations moves X outside it. Convention slips can be avoided without additional experimental work. The other three slips remain within the interval. For C1 and C2, this reflects the moderate instrumental contribution, $G/W = 0.40$, and would change for a narrower diagnostic line (Figure 2).

Second, normalization provides no indication of a slip. All 13 perturbed compositions sum to 100% by construction. In 11 cases, the major element remains within 5% of its baseline fraction. The exceptions are C6 and C8, where a minor constituent is increased severalfold. Normalization strongly constrains the fraction of a dominant constituent, making its apparent agreement a weak test of the calculation. The numerical effects reported here belong to the constructed example and should not be transferred directly to real plasmas. The dependence on width conventions, ionization corrections, and concentration basis is general, but neither the magnitudes, the six-of-nine count, nor the indicator sensitivity is an experimentally established rate. They depend on this composition, line list, plasma parameters, and assigned uncertainty model.

Transfer to an experiment requires identifying which of the same equations and conventions the experimental workflow actually uses. Spatial and temporal gradients, self-absorption, departures from LTE, non-representative ablation, line blending, and instrumental response can add coupled effects absent from this constructed record [12,22]. Changes in matrix, ambient gas or pressure, pulse energy and observation window may therefore change both the size and ordering of the illustrated effects. The example motivates checking those dependencies; it does not provide transferable error bars or detection probabilities. Establishing them would require separate tests over specified materials and acquisition conditions with independent reference information. Section 4.5 reports one such comparison, limited to the instrumental-linewidth step.

4.3. Identifying Slips with a Partial Record

A reader with only the final concentration table cannot identify any of the nine slips. An analyst, or a reader with some intermediate information, can examine three indicators. We evaluated each indicator for every perturbation (Figure 4 and Table S5).

The first indicator compares the electron density implied by the Saha balance of an element observed in two charge states with the density obtained from Stark broadening. For Y, the baseline ratio is 0.99. Input uncertainties alone give a 95% range of 0.54 to 1.82. The indicator clearly identifies the tenfold density slips, whose ratios are 0.10 and 9.9. It identifies the twofold slips only marginally, with ratios of 0.49 and 1.97.

The second indicator is the residual standard deviation of the Boltzmann plot. Its baseline value is 0.03. In this constructed record, the scatter reflects intensity noise alone because the generating atomic data are exact. The uncertainties assigned to the transition probabilities would give a scatter of 0.07 to 0.14. C7 increases the scatter to 0.18, above this range, while the other slips leave this indicator unchanged. Both indicators retain their baseline values when slips occur after plasma parameters have been established, as in C8 and C9.

The third indicator compares the result with a reference value, where available. We propagated input uncertainties through each perturbed calculation, following the procedure an analyst would use after making the slip, and evaluated ζ against the constructed reference. Five slips give $|\zeta| > 2$ for at least one element, while four remain compatible under this criterion. C4 is among the latter: X is 80% too high, but $\zeta = 1.7$ because the propagated uncertainty increases with the result. The outcome also depends on the uncertainty assigned to the method. If only the standard deviation of the mean is used, every slip gives $|\zeta| > 2$, as do U1 to U3. The test then fails to distinguish convention slips from the assigned input uncertainty.

Together, the three indicators flag seven of the nine slips in this record. C1 and C2, the two instrumental-linewidth slips, remain undetected by all three. We examine their effects on electron-density estimates experimentally in Section 4.5. Passing several checks therefore cannot guarantee correct assumptions or calculation choices. Stating the conventions makes them available for direct checking against their sources, but we have not measured analysts' ability to identify the slips. Section 6 and Supplementary Section S8 report reconstruction by three analysts using the supplied code. Their ability to identify seeded defects was not tested.

4.4. Four Experimental Cases at Different Pulse Energies

We applied the reporting record to LuNOR 102 regolith-simulant spectra acquired at the LIBS Discovery facility, CEITEC, Brno University of Technology, with 1064 nm excitation (8 ns, 20 Hz) in ambient air at 1 atm. The four cases correspond to nominal pulse energies of 0.6, 1.3, 3.7 and 7.5 mJ, with 100 single-shot spectra at each energy. We applied the relative radiometric correction once to our raw spectra and used a conventional Saha–Boltzmann calculation [66] with the same 24-line mask, integration rules and atomic data throughout. Central values were obtained deterministically without adjustment to XRF concentrations; Monte Carlo resampling was used only to quantify conditional sampling variation. Supplementary Text S3 documents the calculation, elemental mass-ratio comparisons with XRF, and variation across five non-overlapping 20-shot groups at each energy.

The common fits give apparent temperatures of 12,226–14,591 K. We evaluated partition functions for Mg, Ca, Fe and Ti in stages I–III as finite sums over the available NIST ASD [52] energy levels, permitting population calculations at these temperatures without extrapolation. Separate Ca I and Ca II slopes give 4348–4740 K and 10,522–12,238 K, respectively, showing stage-dependent apparent temperatures. The resulting elemental mass ratios were compared with XRF on the same basis: Mg/Ca was lower, whereas Fe/Ca and Ti/Ca were higher, with differences varying across pulse energies (Table S9). Figure S2 presents the separate imposed-temperature sensitivity calculation, and Figure S3 shows the apparent temperatures across the measured energy settings.

We also fitted the measured spectra with a homogeneous LTE radiation model and partition functions covering 5000–15,000 K (Supplementary Section S11). The nine numerical runs gave fitted temperatures of 10,488–12,740 K and weighted spectral correlations of 0.970–0.980, while the retrieved elemental ratios remained dependent on

energy and initialization. None reached the local convergence tolerances within the allocated evaluation budget, and the radius reached its lower bound in one run.

These cases demonstrate the reporting workflow on measured spectra and comparison with XRF across pulse energies. Energy variation changes several plasma properties together. Section 4.5 examines the instrumental-linewidth effect separately, while Supplementary Section S6.6 places the measured LuNOR 102 widths on the axis of Figure 2.

4.5. Experimental Test of the Instrumental-Linewidth Estimates

The indicators of Section 4.3 do not detect C1 and C2. We therefore compared the calculated linewidth effects in Figure 2 with measurements using hydrogen lines as a separate electron-density diagnostic. The test uses gated spectra of laser-induced plasmas in xenon–hydrogen mixtures recorded with the apparatus described in refs. [67,68]: total pressures of about 100 and 170 hPa, Xe:H_2 ratios from 1:9 to 9:1, a gate width of 500 ns and gate delays from 10 to 3000 ns (93 spectra; Supplementary Text S5). The Xe II 484.43 nm line supplies the nonhydrogenic linewidth for Equation (4), while the Hα and Hβ widths provide density estimates through the hydrogen-line relations [69,70]. Changes in gate delay, pressure and mixing ratio vary the density and the instrumental-to-observed width ratio, G/W, with the same instrument.

The comparison uses three inputs. The instrumental width at 484.43 nm, $G = 0.026 \pm 0.001$ nm, is estimated from the median Gaussian component of Voigt profiles fitted to the 15 narrowest xenon lines. This estimate uses neither hydrogen lines nor a Stark coefficient. The adopted Stark coefficient is the critically evaluated full width of 0.0546 nm at 10^{17} cm^{-3} [49]. The reference density is the geometric mean of the Hα and Hβ estimates. We include the 43 spectra with gate delays of at least 500 ns in which all three lines can be evaluated. Their hydrogen-line densities span 0.31×10^{17} to 2.55×10^{17} cm^{-3}, and G/W spans 0.15–0.62. None of these inputs is adjusted to improve agreement with the calculated curves.

Figure 5 and Table 4 compare the measurements with the calculated effects. Across five bins of G/W, the Stark fraction inferred from the hydrogen densities agrees with the Voigt-consistent curve within 1.4 standard errors. At median G/W values of 0.50 and 0.58, neglecting the instrumental width gives xenon-to-hydrogen density ratios of 1.36 ± 0.05 and 1.61 ± 0.14, compared with calculated factors of 1.36 and 1.55. Quadrature subtraction gives 1.16 ± 0.04 and 1.33 ± 0.10, compared with 1.18 and 1.26. With the Voigt-consistent treatment of Equation (5), the density ratio has a median of 1.02 across the 43 spectra, a central 68% range of 0.91–1.17 and a full range of 0.82–1.67. A two-parameter fit of observed width against hydrogen density gives compatible estimates: a Stark coefficient of 0.0556 ± 0.0025 nm at 10^{17} cm^{-3} and $G = 0.027 \pm 0.002$ nm (Supplementary Section S12.3). This fit uses the same spectra and provides a consistency check. Figure S6B shows the prediction using the independently specified parameters.

This comparison supports the calculated linewidth effects for checkpoints A1 and A2 over the examined density range, for one ionic line in one gas system. Each spectrum integrates 500 ns, and xenon and hydrogen emission need not sample the same region or time. Because the red half of Hα falls between two echelle orders, its width is inferred from the blue half assuming symmetry; the median ratio of Hβ- to Hα-derived density is 0.91. The comparison uses linewidths and does not require relative intensity calibration across wavelengths. The reported bin errors describe scatter and exclude shared uncertainties in the instrumental width, Stark coefficient and hydrogen profile model.

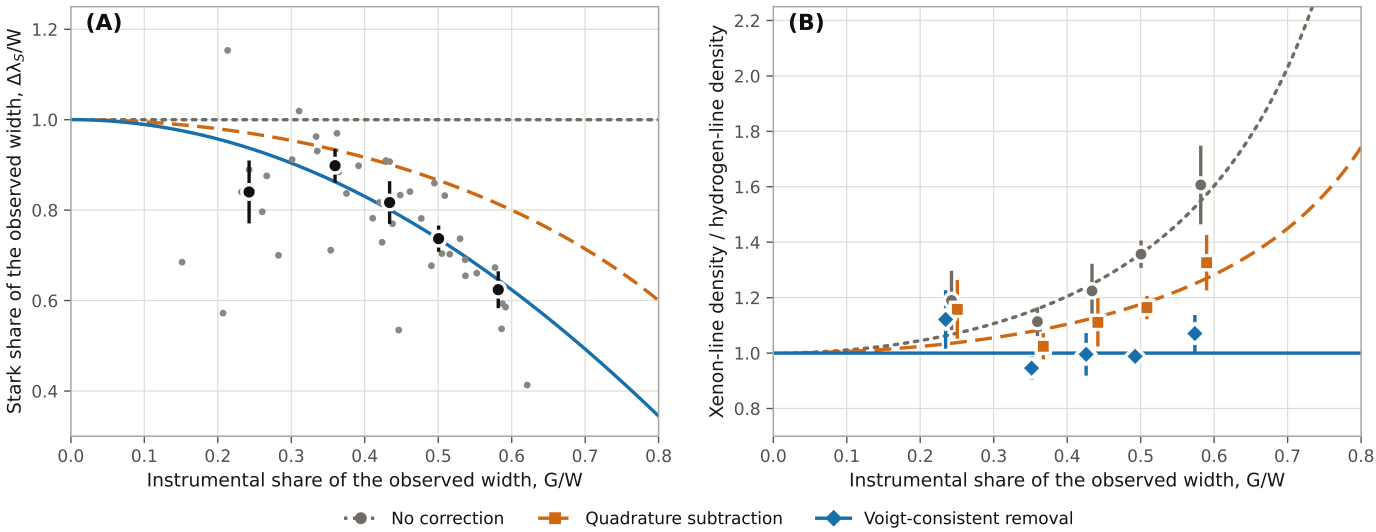


Figure 5. Experimental comparison with the curves of Figure 2 using 43 gated xenon–hydrogen spectra. G is the estimated instrumental width (0.026 nm), and W is the observed width of Xe II 484.43 nm. (**A**) Stark share of the observed width, obtained by scaling the tabulated Stark width to the hydrogen-line electron density and dividing by W. Small gray dots represent individual spectra. Large black circles show bin medians, and black error bars show their approximate standard errors. (**B**) Xenon-line density divided by the hydrogen reference density when instrumental broadening is neglected (circles), subtracted in quadrature (squares), or removed consistently with a Voigt profile using Equation (5) (diamonds). The hydrogen reference is the geometric mean of the Hα and Hβ density estimates. Symbols show bin medians with standard errors as defined in Table 4. The curves are calculated without adjusting parameters to the measurements.

Table 4. Measured and calculated effects of instrumental broadening on electron density from Xe II 484.43 nm in 43 gated xenon–hydrogen spectra. Entries are medians for five bins of G/W, with approximate standard errors of the median ($1.253s/\sqrt{n}$, where s is the sample standard deviation and n the number of spectra). Calculated values from Equation (5) at the median G/W are in parentheses. The Stark share is inferred from the hydrogen-line density and the adopted Stark coefficient. The final three columns give the xenon-line density divided by the hydrogen reference density. Errors describe within-bin scatter and exclude shared model and instrumental uncertainties.

G/W, Median (Range)	Spectra	Stark Share	G Neglected	Quadrature	Voigt-Consistent
0.24 (0.15–0.30)	9	0.84 ± 0.07 (0.94)	1.19 ± 0.11 (1.07)	1.16 ± 0.11 (1.04)	1.12 ± 0.11 (1.00)
0.36 (0.31–0.39)	9	0.90 ± 0.04 (0.86)	1.11 ± 0.05 (1.16)	1.02 ± 0.05 (1.08)	0.95 ± 0.04 (1.00)
0.43 (0.41–0.46)	9	0.82 ± 0.05 (0.80)	1.22 ± 0.10 (1.25)	1.11 ± 0.09 (1.13)	1.00 ± 0.08 (1.00)
0.50 (0.48–0.53)	8	0.74 ± 0.03 (0.74)	1.36 ± 0.05 (1.36)	1.16 ± 0.04 (1.18)	0.99 ± 0.04 (1.00)
0.58 (0.54–0.62)	8	0.62 ± 0.04 (0.65)	1.61 ± 0.14 (1.55)	1.33 ± 0.10 (1.26)	1.07 ± 0.07 (1.00)

Additional measured spectra illustrate how experimental conditions change the importance of instrumental broadening. In pure xenon at 52 hPa, varying the gate delay moves the same line from $G/W = 0.07$ to 0.51. Relative to the Voigt-consistent calculation, neglecting the instrumental width increases the inferred electron density by 0.5% at 10 ns and 37% at 2500 ns; quadrature subtraction leaves an 18% difference at 2500 ns (Figure S8). These differences compare alternative treatments of the measured linewidths. In the LuNOR 102 spectra of Section 4.4, G/W is 0.04–0.05 for Hα, 0.26–0.51 for the Ca II lines, and 0.75–0.96 for neutral Mg, Ca and Fe lines, where the inferred Stark component is particularly sensitive to the instrumental-width estimate (Supplementary Section S6.6, Figure S5). For the pure-xenon spectra, Boltzmann-plot temperatures have standard errors of 13–36% from

the fit alone and change by −19% to +51% when a single line is omitted (Supplementary Section S13), illustrating the temperature sensitivity discussed in Section 3.2.

Reported measurements also illustrate the later checkpoints. For the Cu–Fe alloy of Case B [63], the published electron densities are 2.73×10^{16} cm^{-3} from Stark widths and 3.9×10^{16} cm^{-3} from the Saha–Boltzmann relation. Their ratio, 1.43, falls within the 0.54–1.82 interval of the constructed uncertainty model, although that interval is not an experimental acceptance criterion. The reported copper contents are 18.09 ± 1.26 wt% by CF-LIBS, 21.09 ± 0.84 wt% by ICP-AES and 22.21 ± 1.33 wt% by EDX. Treating the printed uncertainties as independent standard uncertainties gives $\zeta = -2.0$ and -2.2, respectively, from Equation (9). Their coverage is not specified, so these values provide a conditional comparison, not a statistical assessment of agreement. For this binary composition, the 3.0 percentage-point difference from ICP-AES corresponds to relative differences of 14% for copper and 3.8% for iron, illustrating the normalization effect discussed in Section 3.5. For the nominal alloy, conversion from copper mass fraction to mole fraction changes the value from 20.00% to 18.01% (Table 2), demonstrating the importance of an explicitly stated comparison basis. These calculations illustrate reporting conventions without assessing the overall quality of the original study.

For LuNOR 102, the electron densities returned by the Saha–Boltzmann fits are 6–14 times those inferred from the Hα width in the same time-integrated spectra (Table S14), showing a discrepancy between the two density diagnostics. At 0.6 mJ and the imposed 10,000 K, comparing mole ratios directly with XRF mass ratios would change the apparent deviation from −43% to −6% for Mg/Ca and from −4.5% to −31% for Fe/Ca. Thus, a basis error can improve apparent agreement for one ratio while worsening it for another. These comparisons illustrate the consequences of calculation and reporting choices in measured records; broader assessment requires gated measurements on certified materials with a calibrated spectral response, as proposed in Section 6.

5. A Minimum Reporting Record

5.1. Content and Organization

Table 5 separates a core reconstruction record from recommended supporting material. Core items are the numerical inputs and decisions needed to regenerate the claimed output at an explicitly declared boundary, such as line integrals to composition. Reconstructing a spectrum-to-composition claim additionally requires the spectral preprocessing inputs. A field can be marked not applicable with a reason; an unavailable applicable input remains a reporting gap, not a satisfied requirement. For A3, reporting the assessment status is core; an unassessed assumption does not become physically supported by being documented. The proposal is intended for discussion, not as a consensus standard. Table 5 is tailored mainly to classic Boltzmann–Saha CF-LIBS. Columnar-density, Cσ and spectral-simulation approaches use additional model and characterization inputs [16,17,22]. Supplementary Section S9 and Table S11 extend the reporting questions to Cσ, spectral simulation and machine-learning-assisted workflows without assuming identical equations or validation requirements. They distinguish characterization standards, forward-model inputs, trained-model inference and model training. A linewidth diagnostic can be inapplicable, but the alternative route to density or composition must then be stated. Workflow-specific inputs used to obtain the claimed output belong to the core record. Files may be distributed across the article, supplement and repository if their relationships remain explicit.

Table 5. Core and recommended levels of the proposed CF-LIBS reporting record. Core means necessary for the stated reconstruction boundary; recommended items extend auditability or physical and analytical assessment. Neither tier certifies physical validity. A measured quantity required by the chosen model cannot be made optional by moving it to the recommended tier. These core dependencies apply to both study types distinguished in Section 5.1 and Supplementary Table S12.

Scope	Core: Required to Reconstruct the Claimed Calculation	Recommended: Supporting Evidence and Reuse
Context	Sample and acquisition identifiers; laser, gas, pressure, timing, instrument/software version; calculation boundary; input intensities/widths and units; correction, background, integration, deblending and selection rules actually used.	Raw spectra and calibration measurements, spatial/time information and full acquisition logs. Spectral windows become core when preprocessing is reconstructed.
A1	Diagnostic line; observed/component widths used; profile model, instrumental contribution and other broadening treatment; unavailable components explicitly identified.	Measured instrumental line shape, fit covariance and residuals. Instrumental data used for a claimed corrected width are core.
A2	Line list and atomic values as used; source/version; width definition and reference density; ordinate, intensity scale, units, constants, weights and exclusions; fitted temperature/density and numerical route.	Atomic-data accuracy information and correlations, alternative line sets and independent density/temperature checks.
A3	Status of each relevant assumption: assessed, unassessed or not applicable; inputs, criteria and line coverage for any claimed test; self-absorption corrections actually used.	Additional time/spatial diagnostics, optical-depth and ablation studies. Evidence essential to a claimed validation remains essential.
A4	Species intensities/intercepts, partition functions and ionization data; observed/inferred stages; closure set; mole-to-mass conversion, molar masses and sample basis; iteration settings; full-precision empirical coefficients if used.	Alternative initialization/line-set sensitivity, diagnostic trajectories and model comparisons.
A5	Paired reference/results on a common basis; reference provenance; replicate definitions; stated uncertainty method and inputs, or an explicit missing-budget status; agreement criterion and scope.	More independent materials, pellets, days or laboratories; full reference certificates and extended uncertainty/sensitivity analysis.
Execution	Machine-readable inputs, equations or executable calculation, versions, full-precision coefficients/intermediates, expected outputs and numerical tolerances; a manifest linking every claim to files and fields.	Environment lock file/container, automated exporter and broader regression benchmarks.

For the record to be useful, every reported output must be traceable to its inputs. Wherever possible, the calculation producing the principal table should be supplied as code with pinned versions and expected outputs. A correction should create a new version while preserving the evidence behind the published value. These requirements follow established practice for reproducible computation [43] and the FAIR principles for data and research software [38,71]. A compact set of connected tables provides more value than a large archive whose quantities cannot be related. Observed data, inputs used in analysis, and derived results should be retained as separate layers. An executable record also allows later updates. Improved Stark parameters or transition probabilities can be applied to deposited data without repeating the measurement.

The amount of documentation should remain proportionate to the calculation. Some of the most useful entries require little storage or additional effort. Coefficients at full precision, explicit exponents and units, the line list as used, fractions before and after conversion, and paired reference values often occupy only a few kilobytes. Measuring an instrumental profile at the diagnostic wavelength or analyzing additional reference materials is more demanding. The record makes these limitations visible so that their consequences can be assessed.

A copyable JSON template, a structural JSON Schema, and a field-to-checkpoint guide are supplied as Data S4. The schema tests organization and explicit missingness, not physical validity or completeness of a particular scientific model. Supplementary Section S7 distinguishes quantities normally retained during analysis, instrument-dependent exports, new measurements, and information recoverable later. For a handheld user, accessible settings, instrument/software version, replicate results, comparison basis and reference

information can be recorded now; inaccessible intermediate quantities must remain labelled inaccessible. End-to-end reconstruction cannot be claimed when those dependencies are missing.

Reporting depth should also follow the paper's claim (Supplementary Section S10, Table S12). Application-focused studies should identify the implemented method/version, accessible settings, actual input/output record, sample and replicate definitions, comparison basis and limits of access. Method-development studies should additionally document new equations or model training, all adjustable choices, reusable implementation, and evidence supporting their claimed improvement and domain of validity. Both retain the same core dependencies for the calculation they claim to reconstruct. A closed-source application may provide an acquisition-to-output record and empirical performance evidence while leaving internal calculations inaccessible; it must not label those calculations independently reconstructed. These tiers limit reporting effort without waiving evidence needed for an accuracy or generalisation claim.

5.2. Automated Checks

Machine readable records allow automatic checks of internal consistency. These include substitution into the Stark relation, reference density scales, units in the LTE criterion, closure and basis conversions, and deviation arithmetic. The accompanying scripts apply these checks to the constructed record (Code S1) [72]. Values transcribed from published studies and their recalculations are available as Data S2 and Code S2 (version 1.0.0, release tag `published-records-v1.0.0`) in the accompanying GitHub repository [73]. The experimental Saha–Boltzmann calculation is documented in Supplementary Text S3, the spectral fits in Supplementary Section S11, and the linewidth analyses in Supplementary Text S5. The supplied numerical tables and plotting scripts allow the experimental figures to be regenerated. A structural validator checks the organization and explicit missingness of the Data S4 reporting template. These checks verify execution and specified numerical relationships; physical validity and usability by independent analysts require separate evaluation.

Such checks require clear treatment of incomplete information. A test that cannot be performed must retain that status. Numerical tolerances used to compare rounded values describe the matching policy and provide no information about measurement uncertainty. Every transcribed quantity requires verification against its source before the resulting check is treated as evidence.

5.3. Practical Limits and Objections

We consider five objections to this proposal. First, the reporting burden can be substantial. Authors already complete many checklists, and additional requirements can encourage routine statements with little useful content. The proposed record should therefore be proportionate and should use the outputs already produced during analysis. Exporting these quantities directly from analysis software can require less effort than describing them in prose.

Second, guidelines do not ensure compliance. Two surveys of quantitative PCR reporting, covering more than 1700 publications and published four years after the minimum information guidelines, found that essential technical information remained widely absent. Publications citing the guidelines reported it more completely [74]. This experience supports greater emphasis on executable records and automated checks alongside the written checklist.

Third, proprietary software can prevent access to intermediate quantities. Commercial instruments, including handheld systems [4], may use quantification algorithms that the

user cannot inspect. In this case, the record should identify the inaccessible steps. Users can also request export functions from instrument manufacturers. Export availability depends on the instrument and software version; this Perspective does not assume that every commercial system exposes line integrals, fitted components or partition functions. An instrumental profile, radiometric standard measurement or independent reference analysis cannot generally be recreated from a final concentration table. Later reconstruction is possible only where the necessary spectra, settings and calibration information were retained.

Fourth, complete reporting exposes an author to more detailed criticism than a final concentration table alone. Reviewers and editors can address this imbalance by recognizing disclosed limitations as useful evidence and treating undocumented steps as open questions.

Fifth, Table 3 is a methodological synthesis informed by reconstruction experience rather than a systematic assessment of identified studies. It therefore cannot establish the frequency of reporting patterns or support conclusions about individual measurements. The constructed record and its perturbations provide material that readers can examine independently. Section 4.5 provides an experimental comparison of the instrumental-linewidth estimates. Broader independent reconstruction exercises and experimental comparisons across the remaining checkpoints are needed to evaluate the proposal's general applicability.

6. Outlook: Developing Community Practice

The proposed reporting record should be evaluated with the same care as the results it documents. Three lines of work can assess its usefulness, while a fourth concerns future analysis software. Table 6 places these activities, together with actions available to authors and reviewers now, on three time horizons.

Table 6. A staged agenda for evaluating and adopting a CF-LIBS reporting record.

Horizon	Action	Main Participants	Expected Contribution
Now	Include the minimum record in new submissions, beginning with principal numerical claims; state width definitions, reference densities, intensity units, and concentration basis.	Authors	Recoverable principal results at modest cost.
Now	Request missing dependencies by name; distinguish unexamined assumptions from tested assumptions; recognize disclosed limitations.	Reviewers and editors	Targeted requests proportionate to the analysis.
1 to 2 years	Independently reconstruct deposited records and compare what different analysts can recover.	Research groups	Evidence of sufficiency and remaining ambiguity.
1 to 2 years	Develop an open benchmark of complete constructed records and synthetic spectra, including seeded defects, with open source checkers and record exporters.	Method and software developers	Sensitivity and false alarm rates of human and automated checks.
3 to 5 years	Compare laboratories using shared spectra and reference materials, with the full reporting record.	LIBS community and metrology institutes	Identification of choices driving differences between laboratories.
3 to 5 years	Develop community minimum information guidelines and integrate record export into instrument software, including field and planetary instruments.	Community bodies, journals, and instrument manufacturers	A reporting standard maintained by its users.

Independent reconstruction

The first question is whether another analyst can recover the reported outputs from deposited material without informal assistance. Two analysts independently transcribing and reconstructing the same record can distinguish disagreement about the source information from disagreement about arithmetic. Three researchers based in India (Analyst A), the United States (Analyst B) and Germany (Analyst C) checked execution of the supplied program against a fixed numerical record. Their returns documented completion of all five execution stages and passing of the 56 specified checks per analyst (Supplementary Section S8). This exercise supports program execution and numerical agreement using the supplied implementation. Independent implementations, unassisted usability and physical validity require separate assessment. Agreement that an input is missing is itself informative and need not be converted into a judgment of the scientific quality of the study.

Benchmarks with seeded defects

Human and automated checks need records whose status is known. Benchmarks should include complete, correct records and records containing deliberate unit mismatches, missing widths, inconsistent reference densities, rounded slopes, or changes of concentration basis. These materials allow the sensitivity to each defect and the false alarm rate to be measured. Section 4.3 illustrates that otherwise plausible checks can miss plausible slips. The constructed record and its 13 perturbations, with definitions and expected outcomes, provide initial benchmark entries. Shared synthetic spectra would extend this evaluation to line fitting, where we expect larger differences between automated workflows.

Interlaboratory comparisons

Shared measurements provide the next level of evaluation. Existing comparisons and open datasets have demonstrated their value to the LIBS community [39–41]. Laboratories analyzing common spectra and then common reference materials, while retaining the full record, could identify the choices responsible for differences in their results. Repeating a numerical calculation and obtaining compatible measurements under changed conditions are separate achievements that both require assessment. The linewidth comparison should be extended to certified alloys with gated acquisition and a calibrated spectral response.

Automated, machine learning, and autonomous analysis

High throughput CF-LIBS reduces direct analyst involvement and makes initialization and hyperparameters part of the result [24]. Methods using spectral simulation add an optimizer and its settings [23]. Machine learning components introduce further dependencies, including training data and model versions, whether they replace the plasma model or estimate its parameters. Their interpretability also contributes to the evidence supporting the result [9,75]. For mineral identification, supervised learning has also been applied to LIBS spectra acquired under reduced pressure, with interpretable feature selection and estimates of classifier confidence [76]. For these workflows, we recommend a compact diagnostic trace documenting starting conditions, parameter evolution, stopping conditions, and excluded or unresolved lines.

This need is particularly strong for field and planetary instruments [4,5]. An analyst may not inspect each spectrum, reference standards may be unavailable, and a sample may never be measured again. Mission spectra remain archived for decades and are examined by researchers who did not participate in the original instrument work. A reporting record stored with these spectra would allow compositions to be recalculated when atomic data or plasma models improve. We therefore suggest that instrument software export the record by default.

The next few years are likely to bring several CF-LIBS variants rather than one universal algorithm. These may include methods combining one point calibration and machine learning within automated workflows. Comparing their results will require each result to retain its calculation record. Better Stark parameters and transition probabilities may also contribute substantially to improved accuracy. Archived records would allow these improvements to be translated into revised compositions without new measurements.

The first steps can be taken without formal coordination. Authors can document the central numerical claims of their next article. Reviewers can identify a specific missing dependency, and developers can provide record export. This makes it possible to distinguish revisions to a transcription, a convention, a physical model, and an analytical conclusion. The guidelines discussed in the Introduction were developed by practitioners of the respective techniques [32,35]. A CF-LIBS guideline should be developed in the same way, with regular LIBS conferences providing a suitable forum.

7. Conclusions

A reported CF-LIBS concentration follows a sequence of choices that the final composition table does not retain. This Perspective proposes reconstructability of that sequence as an explicit reporting objective. Recovering the calculation is a separate question from establishing the physical validity of its model or its fitness for an analytical purpose. It provides the information needed to examine the physical assumptions and, when reference materials are unavailable, to interpret the analytical result.

The five checkpoints connect linewidth provenance, plasma parameters, model evidence, concentration calculation, and reference comparison. Within the specified hypothetical ternary record, six of nine convention slips move the light minor constituent outside its propagated 95% interval, while all compositions remain normalized. The three indicators together flag seven slips and miss two. These counts and numerical effects belong to the assigned composition, line list, plasma conditions and uncertainty model; the shared-model reconstruction does not establish experimental validity or general detection performance.

The four LuNOR 102 energy cases demonstrate reconstruction from measured spectra and comparison with XRF on a common elemental mass-ratio basis, revealing element- and energy-dependent differences. In 43 gated xenon–hydrogen spectra, the Stark fractions inferred from hydrogen-line densities agree with the calculated Voigt-consistent curve within 1.4 standard errors across five bins spanning G/W values from 0.15 to 0.62. The Voigt-consistent treatment gives a median xenon-to-hydrogen density ratio of 1.02. This comparison provides experimental support for the linewidth estimates for one ionic line in one gas system; the bin errors describe scatter and exclude shared instrumental and model uncertainties.

The proposed core record and recommended extensions make calculation dependencies explicit and provide a template for testing. Three analysts recovered the specified outputs using the supplied code, supporting execution and numerical reconstruction with that implementation. Independent implementations, benchmarks across different datasets, and controlled interlaboratory measurements remain necessary before general sufficiency or performance can be claimed.

Supplementary Materials: The following supporting information can be downloaded at https://www.mdpi.com/article/10.3390/chemosensors14120262/s1. Text S1. Constructed Worked Examples and Reporting Record. Text S2. Reconstructions of Published Records. Text S3. Experimental Reconstruction at Four Pulse Energies. Text S4. Reporting Template and Reconstruction Evaluation. Text S5. Experimental Test of the Linewidth Estimates. Figure S1. Boltzmann plot for the first replicate of the constructed record. The lines show the least squares fit with one common slope

and a separate intercept for each species. The fitted slope corresponds to 9970 K for this replicate. Figure S2. Imposed-temperature sensitivity of elemental mass ratios relative to XRF for the four measured pulse energies, using the original Barklem–Collet table. Within each panel, temperature is imposed and density and elemental intercepts are refitted. The horizontal line marks equality with the reference. Bars give SD across five 20-shot groups. Panels (A)–(D) correspond to 0.6, 1.3, 3.7 and 7.5 mJ. The horizontal axis is a computational sensitivity scenario, not a measured temperature scan. Figure S3. Apparent common-fit and separate stage-slope temperatures at the four nominal pulse energies. Connecting lines guide the eye. The dotted line marks the 10,000 K endpoint of the original Barklem–Collet tabulation. The NIST level sums in Section S6.2 cover the fitted temperatures shown here. Figure S4. Element/Ca mass ratios relative to XRF and fitted temperatures for the two local starts at each measured energy. The separate symbol at 7.5 mJ shows the additional stochastic search. Connecting lines guide the eye. Panels (A)–(D) show Mg/Ca, Fe/Ca, Ti/Ca and temperature, respectively. The same 100-shot mean is used for all searches at a given energy; their differences are not uncertainty intervals. Figure S5. Measured LuNOR 102 line widths on the calculated curves of Figure 2. (A) Stark share of the observed width and (B) overestimate of electron density relative to Voigt-consistent removal, as functions of G/W. Curves: calculated from Equation (5), as in Figure 2. Markers: four groups of measured lines at the centre of their range of G/W; horizontal bars give the range over the four pulse energies and both estimates of G (Table S14). Only the horizontal positions are measured. Circles: ambient-air Hα; squares: reduced-pressure Hα; triangles: Ca II; diamonds: neutral metal lines. Table S14 gives the widths and ranges. Figure S6. Gated xenon–hydrogen spectra (43 spectra). (A) Electron density from Xe II 484.43 nm, with the literature Stark coefficient and Voigt-consistent removal of G, against the electron density from Hα and Hβ. Line: equality. Shaded, for comparison: the 95% range that input uncertainties alone give for the density-ratio indicator of the constructed record (0.54–1.82; Section 4.3). (B) Observed FWHM of Xe II 484.43 nm against the hydrogen density. Solid curve: Equation (5) with the literature Stark coefficient and G = 0.026 nm from the line shape; no parameter is fitted. Dotted line: Stark width alone. Open markers: Gaussian components of the 15 narrowest profiles, whose median is G (dashed line). Grey line: spacing of the wavelength grid, 0.011 nm. Figure S7. Pure xenon at 160 hPa. (A) Boltzmann plot of one spectrum (gate delay 10 ns, 15 Xe II lines; T = 22,418 $\pm$ 3,565 K). (B) Temperature against gate delay. Filled circles: all listed lines. Open circles: spectra whose line list does not contain the 441.48 nm line. Squares: the eight lines common to all nine spectra. Bars: standard error of the Boltzmann fit with all listed lines; the standard errors of the common set are given in Table S16. Curves: single-exponential fits $T_0 \exp(-t/\tau)$, weighted with the standard errors, with decay times τ of 6.3 $\pm$ 1.5 μs (all listed lines) and 6.5 $\pm$ 0.9 μs (common lines); these uncertainties describe the scatter of the points about the curves. The three acquisitions at 10 ns are displaced horizontally for clarity. Figure S8. Pure xenon at 52 hPa. (A) Electron density from Xe II 484.43 nm against gate delay, on a logarithmic scale, with the instrumental width neglected (circles), subtracted in quadrature (squares) or removed consistently with a Voigt profile (diamonds). Lines: single-exponential fits $N_{e0} \exp(-t/\tau)$, which are straight on this scale, with decay times τ of 1.18 $\pm$ 0.19, 1.09 $\pm$ 0.16 and 1.02 $\pm$ 0.14 μs, respectively. At 2500 ns, neglecting the instrumental width and subtracting it in quadrature exceed the Voigt-consistent density by 37% and 18%, respectively. The second row of tick labels gives G/W. (B) Line intensity from the original evaluation against the Voigt-fit area measured in the spectrum, for the 42 lines of four spectra. Line: equality. Shaded: within 25%. Filled markers: signal-to-noise ratio above 30. Table S1. Fraction of the observed FWHM attributed to Stark broadening and the resulting overestimate of electron density for a Lorentzian line convolved with a Gaussian instrumental profile. G is the instrumental FWHM and W the observed FWHM. Values are calculated with Equation (S1); the numerical output is `outputs/table_linewidth.csv`. Table S2. Line list and intensities for the five replicates of the constructed record. The level energies, statistical weights, and transition probabilities are invented values for hypothetical elements and do not correspond to real transitions. Intensities are expressed in photon units on an arbitrary common scale. The data file is `record/line_intensities.csv`. Table S3. Reconstructed composition and comparison with the constructed reference. The reference is the nominal mass composition; reconstructed mole and mass percentages are arithmetic means

of the five replicate estimates. δ is the signed relative deviation of the mean; RSD is the relative standard deviation of five replicates; u_{rep} is the standard deviation of the mean; u_{in} is the standard uncertainty from Monte Carlo propagation of the input uncertainties; and u_{c} is their combined standard uncertainty, corresponding to u_m in Equation (9). The 95% interval spans the 2.5th to 97.5th percentiles of the Monte Carlo distribution, and ζ is the normalized deviation. Fractions, uncertainties, and intervals are expressed as mass percentages, except for the column identified as mole percentages. Table S4. Effects of individual perturbations of the constructed record. The N_{e} and T columns give the perturbed plasma parameter divided by its baseline value. The X, Y, and Z columns give the recovered mean mass fraction divided by its baseline value of 5.982%, 91.034%, and 2.984%, respectively. CP identifies the checkpoint at which the perturbation acts. Fractions sum to 100% in every scenario. The data file is `outputs/seeded_defects.csv`. Table S5. Indicators that could identify each perturbation in Table S4. Density ratio is the electron density from the Saha balance of Y divided by the Stark density. Scatter is the residual standard deviation of the Boltzmann plot. ζ is the normalized deviation from the constructed reference with input uncertainties propagated through the perturbed calculation. Flags are D for a density ratio outside its 95% range, S for scatter above its 95% range, and R for $|\zeta| > 2$ for at least one element. Table S6. Central concentrations from Table 6 of El-Saeed et al. [62] and signed relative deviations, $\delta = 100(C_m - C_r)/C_r$. Concentrations are in ppm as printed; the two estimates use electron density and temperature, respectively. Table S7. Inputs from Table 1 of Fayyaz et al. [63] for its intensity-ratio comparison. Intensities are in reported arbitrary units. The common Cu upper-level energy is used for both Cu lines. Table S8. Reconstruction provenance for the three published records. No experimental uncertainty or missing spectral quantity is inferred from a successful arithmetic check. Table S9. Elemental mass ratios for LuNOR 102 at four pulse energies, calculated from the fixed 24-line set using NIST level-sum partition functions at the fitted temperatures. Central values use the 100-shot mean line areas. Parentheses give the standard deviation (SD) of ratios obtained by separately fitting five non-overlapping 20-shot groups, with shared atomic and model inputs fixed. XRF values are expressed on the same elemental mass-ratio basis. Table S10. Practical routes for completing a reporting record. Availability depends on the actual instrument and software. No universal commercial export capability is assumed. Table S11. Workflow-specific additions to the core record. Required inputs depend on the calculation being reconstructed; these reporting suggestions do not establish performance or physical validity. Table S12. Proposed reporting expectations by study purpose. These are claim-dependent suggestions, not validated community requirements. Application papers claiming a new algorithm or broad performance improvement also need the corresponding method-development evidence. Table S13. Spectral-fitting results for the four measured 100-shot means. Starts 1 and 2 denote local refinements from recorded initial vectors; MC denotes the additional stochastic search at 7.5 mJ. All local searches reached the evaluation limit without satisfying the convergence tolerances. Element/Ca entries are mass ratios; the XRF counterparts are 0.7487, 1.9379 and 0.4300. Q is the spectral objective. No uncertainty interval is assigned. Table S14. Observed widths W (FWHM, nm) of eleven lines in the 100-shot mean spectra of LuNOR 102 at the four pulse energies, working limits for the instrumental width G at each line, and the resulting range of G/W. Lower estimate: Gaussian model of Section S11. Upper estimate: width of the same line in the reduced-pressure spectrum; for Hα, the Dα line of the deuterium lamp. For Hα at reduced pressure the two entries of W are the half-maximum width and the width of a Voigt fit. The line-by-line file with both width measures is part of Data S6. Electron densities from Hα are 3.21, 2.88, 2.88 and 2.98 $\times$ 10^{17} cm^{-3} in increasing energy order. Table S15. The 93 gated xenon–hydrogen spectra (gate width 500 ns). W: FWHM of the Voigt fit to Xe II 484.43 nm (nm); S/N: fitted peak divided by the standard deviation of the fit residuals; Gauss: Gaussian component of the same fit (nm); G/W with G = 0.0258 nm; electron densities in 10^{17} cm^{-3} from Hα (Equation (S10)), Hβ (Equation (S11)), their geometric mean, and the xenon line with Voigt-consistent removal of G (Equations (4) and (S1)); ratio of the xenon-line density to the hydrogen density. Use: C, in the comparison of Section S12.4 (43 spectra); G, used for the instrumental width (15 spectra). Entries are blank where a line could not be evaluated. Table S16. Boltzmann-plot temperatures of pure xenon, recalculated from the 20 Xe II line lists of the original evaluation. n: number of lines. T

± standard error of the fit, and the standard error in percent. Leave-one-out: range of T when one line at a time is left out. Common set: T from the lines common to all spectra of the same pressure (six lines at 52 and 96 hPa, eight at 160 hPa). Recorded: temperature recorded with the line list, where available. Table S17. Pure xenon at 52 hPa (300 accumulations, gate width 500 ns). W and Gauss: FWHM and Gaussian component of the Voigt fit to Xe II 484.43 nm (nm). G/W with G = 0.0258 nm. Electron densities in 10^{17} cm^{-3} under the three treatments of G, with the excess over the Voigt-consistent value. Temperatures from the line intensities of the original evaluation and from the line areas measured in the spectra, each with the standard error of the fit; n: number of lines. The Supplementary Materials cite Refs. [17,18,48,49,52,53,57,61–70,77–81].

Author Contributions: Conceptualization, H.S. and M.F.; methodology, H.S.; software, H.S.; validation, H.S. and M.F.; formal analysis, H.S.; investigation and data acquisition, J.B., P.P. and J.K.; data curation, H.S.; writing—original draft preparation, H.S.; writing—review and editing, H.S., P.K., J.S., J.B., P.P., J.K. and M.F.; visualization, H.S.; supervision, H.S.; funding acquisition, J.K., P.K. and M.F. All authors have read and agreed to the published version of the manuscript.

Funding: This work was supported by the National Centre of Competence for Aerospace under project TN02000009/11. The authors further acknowledge support from the Czech Science Foundation (GAČR), project No. 26-22475K.

Data Availability Statement: The constructed record, transcribed literature inputs, experimental result tables, figure data, reporting templates, analyst execution records, and analysis and plotting scripts supporting this study are available in the accompanying GitHub repository [73]. The original Code S1 release is archived at https://doi.org/10.5281/zenodo.23196815.

Conflicts of Interest: The authors declare no conflicts of interest.

Abbreviations

CF-LIBS	Calibration free laser induced breakdown spectroscopy
EDX	Energy-dispersive X-ray spectroscopy
FAIR	Findable, accessible, interoperable, reusable
FWHM	Full width at half maximum
HWHM	Half width at half maximum
ICP-AES	Inductively coupled plasma atomic emission spectroscopy
IUPAC	International Union of Pure and Applied Chemistry
LA-ICP-MS	Laser ablation inductively coupled plasma mass spectrometry
LIBS	Laser induced breakdown spectroscopy
LTE	Local thermodynamic equilibrium
NIST	National Institute of Standards and Technology
PCR	Polymerase chain reaction
RSD	Relative standard deviation
XRF	X-ray fluorescence

References

1. Hahn, D.W.; Omenetto, N. Laser-induced breakdown spectroscopy (LIBS), part II: Review of instrumental and methodological approaches to material analysis and applications to different fields. *Appl. Spectrosc.* **2012**, *66*, 347–419. https://doi.org/10.1366/11-06574.
2. Fortes, F.J.; Moros, J.; Lucena, P.; Cabalín, L.M.; Laserna, J.J. Laser-induced breakdown spectroscopy. *Anal. Chem.* **2013**, *85*, 640–669. https://doi.org/10.1021/ac303220r.
3. Palleschi, V.; Legnaioli, S.; Poggialini, F.; Bredice, F.O.; Urbina, I.A.; Lellouche, N.; Messaoud Aberkane, S. Laser-induced breakdown spectroscopy. *Nat. Rev. Methods Primers* **2025**, *5*, 17. https://doi.org/10.1038/s43586-025-00388-w.
4. Senesi, G.S.; Harmon, R.S.; Hark, R.R. Field-portable and handheld laser-induced breakdown spectroscopy: Historical review, current status and future prospects. *Spectrochim. Acta Part B At. Spectrosc.* **2021**, *175*, 106013. https://doi.org/10.1016/j.sab.2020.106013.

5. Saeidfirozeh, H.; Kubelík, P.; Laitl, V.; Křivková, A.; Vrábel, J.; Rammelkamp, K.; Schröder, S.; Gornushkin, I.B.; Képeš, E.; Žabka, J.; et al. Laser-induced breakdown spectroscopy in space applications: Review and prospects. *TrAC Trends Anal. Chem.* **2024**, *181*, 117991. https://doi.org/10.1016/j.trac.2024.117991.
6. El Haddad, J.; Canioni, L.; Bousquet, B. Good practices in LIBS analysis: Review and advices. *Spectrochim. Acta Part B At. Spectrosc.* **2014**, *101*, 171–182. https://doi.org/10.1016/j.sab.2014.08.039.
7. Motto-Ros, V.; Syvilay, D.; Bassel, L.; Negre, E.; Trichard, F.; Pelascini, F.; El Haddad, J.; Harhira, A.; Moncayo, S.; Picard, J.; et al. Critical aspects of data analysis for quantification in laser-induced breakdown spectroscopy. *Spectrochim. Acta Part B At. Spectrosc.* **2018**, *140*, 54–64. https://doi.org/10.1016/j.sab.2017.12.004.
8. Wang, Z.; Afgan, M.S.; Gu, W.; Song, Y.; Wang, Y.; Hou, Z.; Song, W.; Li, Z. Recent advances in laser-induced breakdown spectroscopy quantification: From fundamental understanding to data processing. *TrAC Trends Anal. Chem.* **2021**, *143*, 116385. https://doi.org/10.1016/j.trac.2021.116385.
9. Hao, Z.; Liu, K.; Lian, Q.; Song, W.; Hou, Z.; Zhang, R.; Wang, Q.; Sun, C.; Li, X.; Wang, Z. Machine learning in laser-induced breakdown spectroscopy: A review. *Front. Phys.* **2024**, *19*, 62501. https://doi.org/10.1007/s11467-024-1427-2.
10. Zhang, K.; Ji, J.; Liu, Z.; Hou, Z.; Wang, Z. Improvement of laser-induced breakdown spectroscopy quantitative performance using minimizing signal uncertainty as signal optimization target: Taking the ambient pressure as an example. *Chemosensors* **2024**, *12*, 277. https://doi.org/10.3390/chemosensors12120277.
11. Ciucci, A.; Corsi, M.; Palleschi, V.; Rastelli, S.; Salvetti, A.; Tognoni, E. New procedure for quantitative elemental analysis by laser-induced plasma spectroscopy. *Appl. Spectrosc.* **1999**, *53*, 960–964. https://doi.org/10.1366/0003702991947612.
12. Tognoni, E.; Cristoforetti, G.; Legnaioli, S.; Palleschi, V. Calibration-free laser-induced breakdown spectroscopy: State of the art. *Spectrochim. Acta Part B At. Spectrosc.* **2010**, *65*, 1–14. https://doi.org/10.1016/j.sab.2009.11.006.
13. Bulajic, D.; Corsi, M.; Cristoforetti, G.; Legnaioli, S.; Palleschi, V.; Salvetti, A.; Tognoni, E. A procedure for correcting self-absorption in calibration free-laser induced breakdown spectroscopy. *Spectrochim. Acta Part B At. Spectrosc.* **2002**, *57*, 339–353. https://doi.org/10.1016/S0584-8547(01)00398-6.
14. Sun, L.; Yu, H. Correction of self-absorption effect in calibration-free laser-induced breakdown spectroscopy by an internal reference method. *Talanta* **2009**, *79*, 388–395. https://doi.org/10.1016/j.talanta.2009.03.066.
15. Rezaei, F.; Cristoforetti, G.; Tognoni, E.; Legnaioli, S.; Palleschi, V.; Safi, A. A review of the current analytical approaches for evaluating, compensating and exploiting self-absorption in laser induced breakdown spectroscopy. *Spectrochim. Acta Part B At. Spectrosc.* **2020**, *169*, 105878. https://doi.org/10.1016/j.sab.2020.105878.
16. Cristoforetti, G.; Tognoni, E. Calculation of elemental columnar density from self-absorbed lines in laser-induced breakdown spectroscopy: A resource for quantitative analysis. *Spectrochim. Acta Part B At. Spectrosc.* **2013**, *79–80*, 63–71. https://doi.org/10.1016/j.sab.2012.11.010.
17. Aragón, C.; Aguilera, J.A. CSigma graphs: A new approach for plasma characterization in laser-induced breakdown spectroscopy. *J. Quant. Spectrosc. Radiat. Transf.* **2014**, *149*, 90–102. https://doi.org/10.1016/j.jqsrt.2014.07.026.
18. Aguilera, J.A.; Aragón, C. New procedure for CSigma laser induced breakdown spectroscopy addressing the laser-induced plasma inhomogeneity. *Spectrochim. Acta Part B At. Spectrosc.* **2024**, *217*, 106969. https://doi.org/10.1016/j.sab.2024.106969.
19. Cavalcanti, G.H.; Teixeira, D.V.; Legnaioli, S.; Lorenzetti, G.; Pardini, L.; Palleschi, V. One-point calibration for calibration-free laser-induced breakdown spectroscopy quantitative analysis. *Spectrochim. Acta Part B At. Spectrosc.* **2013**, *87*, 51–56. https://doi.org/10.1016/j.sab.2013.05.016.
20. Luo, T.; Huang, W.; Chen, R.; Chen, F.; Chen, J.; Hu, Z.; Nie, J. Rapid high-accuracy quantitative analysis of water hardness by combination of one-point calibration laser-induced breakdown spectroscopy and aerosolization. *Chemosensors* **2025**, *13*, 271. https://doi.org/10.3390/chemosensors13080271.
21. Zhao, N.; Luo, Z.; Wang, B.; Lin, R.; Zheng, S.; Ma, S.; Li, K.; Jiang, E.; Li, J.; Zhang, Q. Multi-element determination in soil using laser-induced breakdown spectroscopy with only one internal reference element by one-point calibration. *J. Anal. At. Spectrom.* **2026**, *41*, 190–198. https://doi.org/10.1039/D5JA00206K.
22. Hermann, J.; Gerhard, C.; Burger, M.; Craciun, V.; Pelascini, F. Progress in calibration-free laser-induced breakdown spectroscopy. *Spectrochim. Acta Part B At. Spectrosc.* **2023**, *200*, 106595. https://doi.org/10.1016/j.sab.2022.106595.
23. Egerland, C.H.; Rammelkamp, K.; Clavé, E.; Lomashvili, A.; Hansen, P.B.; Seel, F.; Schröder, S.; Hübers, H.W. Simulation-based calibration-free laser-induced breakdown spectroscopy using gradient optimization. *Spectrochim. Acta Part B At. Spectrosc.* **2026**, *246*, 107635. https://doi.org/10.1016/j.sab.2026.107635.
24. Matsumura, T.; Takahashi, T.; Nagata, K.; Ando, Y.; Yada, A.; Thornton, B.; Kuwatani, T. High-throughput calibration-free laser-induced breakdown spectroscopy. *ACS Earth Space Chem.* **2024**, *8*, 1259–1271. https://doi.org/10.1021/acsearthspacechem.4c00067.
25. Herrera, K.K.; Tognoni, E.; Omenetto, N.; Smith, B.W.; Winefordner, J.D. Semi-quantitative analysis of metal alloys, brass and soil samples by calibration-free laser-induced breakdown spectroscopy: Recent results and considerations. *J. Anal. At. Spectrom.* **2009**, *24*, 413–425. https://doi.org/10.1039/B820493D.

26. Zhang, N.; Ou, T.; Wang, M.; Lin, Z.; Lv, C.; Qin, Y.; Li, J.; Yang, H.; Zhao, N.; Zhang, Q. A brief review of calibration-free laser-induced breakdown spectroscopy. *Front. Phys.* **2022**, *10*, 887171. https://doi.org/10.3389/fphy.2022.887171.
27. Poggialini, F.; Campanella, B.; Cocciaro, B.; Lorenzetti, G.; Palleschi, V.; Legnaioli, S. Catching up on calibration-free LIBS. *J. Anal. At. Spectrom.* **2023**, *38*, 1751–1771. https://doi.org/10.1039/D3JA00130J.
28. Tognoni, E.; Cristoforetti, G.; Legnaioli, S.; Palleschi, V.; Salvetti, A.; Mueller, M.; Panne, U.; Gornushkin, I. A numerical study of expected accuracy and precision in calibration-free laser-induced breakdown spectroscopy in the assumption of ideal analytical plasma. *Spectrochim. Acta Part B At. Spectrosc.* **2007**, *62*, 1287–1302. https://doi.org/10.1016/j.sab.2007.10.005.
29. Taleb, A.; Motto-Ros, V.; Carru, M.J.; Axente, E.; Craciun, V.; Pelascini, F.; Hermann, J. Measurement error due to self-absorption in calibration-free laser-induced breakdown spectroscopy. *Anal. Chim. Acta* **2021**, *1185*, 339070. https://doi.org/10.1016/j.aca.2021.339070.
30. Völker, T.; Gornushkin, I.B. Importance of physical units in the Boltzmann plot method. *J. Anal. At. Spectrom.* **2022**, *37*, 1972–1974. https://doi.org/10.1039/D2JA00241H.
31. Völker, T.; Gornushkin, I.B. Mass and mole fractions in calibration-free LIBS. *J. Anal. At. Spectrom.* **2024**, *39*, 1030–1032. https://doi.org/10.1039/D4JA00028E.
32. Horstwood, M.S.A.; Košler, J.; Gehrels, G.; Jackson, S.E.; McLean, N.M.; Paton, C.; Pearson, N.J.; Sircombe, K.; Sylvester, P.; Vermeesch, P.; et al. Community-derived standards for LA-ICP-MS U-(Th-)Pb geochronology—Uncertainty propagation, age interpretation and data reporting. *Geostand. Geoanal. Res.* **2016**, *40*, 311–332. https://doi.org/10.1111/j.1751-908X.2016.00379.x.
33. Major, G.H.; Avval, T.G.; Moeini, B.; Pinto, G.; Shah, D.; Jain, V.; Carver, V.; Skinner, W.; Gengenbach, T.R.; Easton, C.D.; et al. Assessment of the frequency and nature of erroneous X-ray photoelectron spectroscopy analyses in the scientific literature. *J. Vac. Sci. Technol. A* **2020**, *38*, 061204. https://doi.org/10.1116/6.0000685.
34. Major, G.H.; Clark, B.M.; Cayabyab, K.; Engel, N.; Easton, C.D.; Čechal, J.; Baer, D.R.; Terry, J.; Linford, M.R. Insufficient reporting of X-ray photoelectron spectroscopy instrumental and peak fitting parameters (metadata) in the scientific literature. *J. Vac. Sci. Technol. A* **2023**, *41*, 043201. https://doi.org/10.1116/6.0002714.
35. Bustin, S.A.; Benes, V.; Garson, J.A.; Hellemans, J.; Huggett, J.; Kubista, M.; Mueller, R.; Nolan, T.; Pfaffl, M.W.; Shipley, G.L.; et al. The MIQE guidelines: Minimum information for publication of quantitative real-time PCR experiments. *Clin. Chem.* **2009**, *55*, 611–622. https://doi.org/10.1373/clinchem.2008.112797.
36. Hanson, R.M.; Jeannerat, D.; Archibald, M.; Bruno, I.J.; Chalk, S.J.; Davies, A.N.; Lancashire, R.J.; Lang, J.; Rzepa, H.S. IUPAC specification for the FAIR management of spectroscopic data in chemistry (IUPAC FAIRSpec)—Guiding principles. *Pure Appl. Chem.* **2022**, *94*, 623–636. https://doi.org/10.1515/pac-2021-2009.
37. Archibald, M.; Bruno, I.J.; Chalk, S.J.; Davies, A.N.; Hanson, R.M.; Kuhn, S.; Lancashire, R.J.; Rzepa, H.S. FAIRSpec-ready spectroscopic data collections—Advice for researchers, authors, and data managers (IUPAC Technical Report). *Pure Appl. Chem.* **2025**, *97*, 1479–1510. https://doi.org/10.1515/pac-2025-0409.
38. Wilkinson, M.D.; Dumontier, M.; Aalbersberg, I.J.; Appleton, G.; Axton, M.; Baak, A.; Blomberg, N.; Boiten, J.W.; da Silva Santos, L.B.; Bourne, P.E.; et al. The FAIR Guiding Principles for scientific data management and stewardship. *Sci. Data* **2016**, *3*, 160018. https://doi.org/10.1038/sdata.2016.18.
39. Völker, T.; Wilsch, G.; Gornushkin, I.B.; Kratochvilová, L.; Pořízka, P.; Kaiser, J.; Millar, S.; Galbács, G.; Palásti, D.J.; Janovszky, P.M.; et al. Interlaboratory comparison for quantitative chlorine analysis in cement pastes with laser induced breakdown spectroscopy. *Spectrochim. Acta Part B At. Spectrosc.* **2023**, *202*, 106632. https://doi.org/10.1016/j.sab.2023.106632.
40. Képeš, E.; Vrábel, J.; Střítežská, S.; Pořízka, P.; Kaiser, J. Benchmark classification dataset for laser-induced breakdown spectroscopy. *Sci. Data* **2020**, *7*, 53. https://doi.org/10.1038/s41597-020-0396-8.
41. Vrábel, J.; Képeš, E.; Duponchel, L.; Motto-Ros, V.; Fabre, C.; Connemann, S.; Schreckenberg, F.; Prasse, P.; Riebe, D.; Junjuri, R.; et al. Classification of challenging laser-induced breakdown spectroscopy soil sample data—EMSLIBS contest. *Spectrochim. Acta Part B At. Spectrosc.* **2020**, *169*, 105872. https://doi.org/10.1016/j.sab.2020.105872.
42. Duponchel, L.; Fabre, C.; Bousquet, B.; Motto-Ros, V. Statistical comparison of predictive models for quantitative analysis and classification in the framework of LIBS spectroscopy: A tutorial. *Spectrochim. Acta Part B At. Spectrosc.* **2023**, *208*, 106776. https://doi.org/10.1016/j.sab.2023.106776.
43. Sandve, G.K.; Nekrutenko, A.; Taylor, J.; Hovig, E. Ten simple rules for reproducible computational research. *PLoS Comput. Biol.* **2013**, *9*, e1003285. https://doi.org/10.1371/journal.pcbi.1003285.
44. Joint Committee for Guides in Metrology. *International Vocabulary of Metrology—Basic and General Concepts and Associated Terms (VIM)*, 3rd ed.; JCGM 200:2012; BIPM: Sèvres, France, 2012. https://doi.org/10.59161/JCGM200-2012.
45. *ISO 5725-1:2023*; Accuracy (Trueness and Precision) of Measurement Methods and Results—Part 1: General Principles and Definitions. ISO: Geneva, Switzerland, 2023.
46. Aragón, C.; Aguilera, J.A. Characterization of laser induced plasmas by optical emission spectroscopy: A review of experiments and methods. *Spectrochim. Acta Part B At. Spectrosc.* **2008**, *63*, 893–916. https://doi.org/10.1016/j.sab.2008.05.010.
47. Griem, H.R. *Spectral Line Broadening by Plasmas*; Academic Press: New York, NY, USA, 1974.

48. Olivero, J.J.; Longbothum, R.L. Empirical fits to the Voigt line width: A brief review. *J. Quant. Spectrosc. Radiat. Transf.* **1977**, *17*, 233–236. https://doi.org/10.1016/0022-4073(77)90161-3.
49. Konjević, N.; Lesage, A.; Fuhr, J.R.; Wiese, W.L. Experimental Stark widths and shifts for spectral lines of neutral and ionized atoms (a critical review of selected data for the period 1989 through 2000). *J. Phys. Chem. Ref. Data* **2002**, *31*, 819–927. https://doi.org/10.1063/1.1486456.
50. Sahal-Bréchot, S.; Dimitrijević, M.S.; Moreau, N.; Ben Nessib, N. The STARK-B database VAMDC node: A repository for spectral line broadening and shifts due to collisions with charged particles. *Phys. Scr.* **2015**, *90*, 054008. https://doi.org/10.1088/0031-8949/90/5/054008.
51. Gigosos, M.A.; Cardeñoso, V. New plasma diagnosis tables of hydrogen Stark broadening including ion dynamics. *J. Phys. B At. Mol. Opt. Phys.* **1996**, *29*, 4795–4838. https://doi.org/10.1088/0953-4075/29/20/029.
52. Kramida, A.; Ralchenko, Yu.; Reader, J.; NIST ASD Team. *NIST Atomic Spectra Database (Version 5.12)*; National Institute of Standards and Technology: Gaithersburg, MD, USA, 2024. Available online: https://physics.nist.gov/asd (accessed on 2 October 2026). https://doi.org/10.18434/T4W30F.
53. Mohr, P.J.; Newell, D.B.; Taylor, B.N.; Tiesinga, E. CODATA recommended values of the fundamental physical constants: 2022. *Rev. Mod. Phys.* **2025**, *97*, 025002. https://doi.org/10.1103/RevModPhys.97.025002.
54. Hahn, D.W.; Omenetto, N. Laser-induced breakdown spectroscopy (LIBS), part I: Review of basic diagnostics and plasma–particle interactions: Still-challenging issues within the analytical plasma community. *Appl. Spectrosc.* **2010**, *64*, 335A–366A. https://doi.org/10.1366/000370210793561691.
55. McWhirter, R.W.P. Spectral intensities. In *Plasma Diagnostic Techniques*; Huddlestone, R.H., Leonard, S.L., Eds.; Academic Press: New York, NY, USA, 1965; pp. 201–264.
56. Cristoforetti, G.; De Giacomo, A.; Dell'Aglio, M.; Legnaioli, S.; Tognoni, E.; Palleschi, V.; Omenetto, N. Local thermodynamic equilibrium in laser-induced breakdown spectroscopy: Beyond the McWhirter criterion. *Spectrochim. Acta Part B At. Spectrosc.* **2010**, *65*, 86–95. https://doi.org/10.1016/j.sab.2009.11.005.
57. Prohaska, T.; Irrgeher, J.; Benefield, J.; Böhlke, J.K.; Chesson, L.A.; Coplen, T.B.; Ding, T.; Dunn, P.J.H.; Gröning, M.; Holden, N.E.; et al. Standard atomic weights of the elements 2021 (IUPAC Technical Report). *Pure Appl. Chem.* **2022**, *94*, 573–600. https://doi.org/10.1515/pac-2019-0603.
58. Joint Committee for Guides in Metrology. *Evaluation of Measurement Data—Guide to the Expression of Uncertainty in Measurement*; JCGM 100:2008; BIPM: Sèvres, France, 2008. https://doi.org/10.59161/JCGM100-2008E.
59. Cantwell, H. (Ed.) Eurachem Guide: The Fitness for Purpose of Analytical Methods—A Laboratory Guide to Method Validation and Related Topics, 3rd ed.; Eurachem, 2025. Available online: https://www.eurachem.org/index.php/publications/guides/mv (accessed on 2 October 2026).
60. Thompson, M.; Ellison, S.L.R.; Wood, R. Harmonized guidelines for single-laboratory validation of methods of analysis (IUPAC Technical Report). *Pure Appl. Chem.* **2002**, *74*, 835–855. https://doi.org/10.1351/pac200274050835.
61. *ISO 13528:2022*; Statistical Methods for Use in Proficiency Testing by Interlaboratory Comparison. ISO: Geneva, Switzerland, 2022.
62. El-Saeed, M.; Tawfik, W.; Khalil, A.A.; Mubarak, M.; Fikry, M. Calibration-free picosecond LIPS for quantifying heavy metals in soils near Egyptian industrial sites. *Sci. Rep.* **2025**, *15*, 19949. https://doi.org/10.1038/s41598-025-04395-5.
63. Fayyaz, A.; Iqbal, J.; Asghar, H.; Alrebdi, T.A.; Alshehri, A.M.; Ahmed, W.; Ahmed, N. Spectroscopical characterization of copper–iron (Cu-Fe) alloy plasma using LIBS, ICP-AES, and EDX. *Metals* **2023**, *13*, 1188. https://doi.org/10.3390/met13071188.
64. Aldakheel, R.; Gondal, M.; Almessiere, M.; Nasr, M.; Rehan, I.; Adel, F. Rapid qualitative and quantitative vital nutrient contents in high-altitude cultivated folklore herbal medicinal Costus roots using calibration-free LIBS. *Arab. J. Chem.* **2024**, *17*, 105941. https://doi.org/10.1016/j.arabjc.2024.105941.
65. Joint Committee for Guides in Metrology. *Evaluation of Measurement Data—Supplement 1 to the "Guide to the Expression of Uncertainty in Measurement"—Propagation of Distributions Using a Monte Carlo Method*; JCGM 101:2008; BIPM: Sèvres, France, 2008. https://doi.org/10.59161/JCGM101-2008.
66. Aguilera, J.; Aragón, C. Multi-element Saha–Boltzmann and Boltzmann plots in laser-induced plasmas. *Spectrochim. Acta Part B At. Spectrosc.* **2007**, *62*, 378–385. https://doi.org/10.1016/j.sab.2007.03.024.
67. Saeidfirozeh, H.; Myakalwar, A.K.; Kubelík, P.; Ghaderi, A.; Laitl, V.; Petera, L.; Rimmer, P.B.; Shorttle, O.; Heays, A.N.; Křivková, A.; et al. ANN-LIBS analysis of mixture plasmas: Detection of xenon. *J. Anal. At. Spectrom.* **2022**, *37*, 1815–1823. https://doi.org/10.1039/d2ja00132b.
68. Shorttle, O.; Saeidfirozeh, H.; Rimmer, P.B.; Laitl, V.; Kubelík, P.; Petera, L.; Ferus, M. Impact sculpting of the early martian atmosphere. *Sci. Adv.* **2024**, *10*, eadm9921. https://doi.org/10.1126/sciadv.adm9921.
69. Gigosos, M.A.; Gonzalez, M.A.; Cardenoso, V. Computer simulated Balmer-alpha,-beta and-gamma Stark line profiles for non-equilibrium plasmas diagnostics. *Spectrochim. Acta Part B At. Spectrosc.* **2003**, *58*, 1489–1504. https://doi.org/10.1016/S0584-8547(03)00097-1.

70. Konjević, N.; Ivković, M.; Sakan, N. Hydrogen Balmer lines for low electron number density plasma diagnostics. *Spectrochim. Acta Part B At. Spectrosc.* **2012**, *76*, 16–26. https://doi.org/10.1016/j.sab.2012.06.026.
71. Barker, M.; Chue Hong, N.P.; Katz, D.S.; Lamprecht, A.L.; Martinez-Ortiz, C.; Psomopoulos, F.; Harrow, J.; Castro, L.J.; Gruenpeter, M.; Martinez, P.A.; et al. Introducing the FAIR Principles for research software. *Sci. Data* **2022**, *9*, 622. https://doi.org/10.1038/s41597-022-01710-x.
72. Saeidfirozeh, H. Code S1: Constructed Examples and Reporting Record for the CF LIBS Perspective. Software, Version 1.0.0. Zenodo, 2026. Available online: https://doi.org/10.5281/zenodo.23196815 (accessed on 6 October 2026).
73. Saeidfirozeh, H. CF-LIBS Reproducibility Audit. GitHub Repository. 2026. Available online: https://github.com/homasf/cf-libs-repro-audit (accessed on 7 October 2026).
74. Bustin, S.A.; Benes, V.; Garson, J.A.; Hellemans, J.; Huggett, J.; Kubista, M.; Mueller, R.; Nolan, T.; Pfaffl, M.W.; Shipley, G.L.; et al. The need for transparency and good practices in the qPCR literature. *Nat. Methods* **2013**, *10*, 1063–1067. https://doi.org/10.1038/nmeth.2697.
75. Képeš, E.; Saeidfirozeh, H.; Laitl, V.; Vrábel, J.; Kubelík, P.; Pořízka, P.; Ferus, M.; Kaiser, J. Interpreting neural networks trained to predict plasma temperature from optical emission spectra. *J. Anal. At. Spectrom.* **2024**, *39*, 1160–1174. https://doi.org/10.1039/D3JA00363A.
76. Saeidfirozeh, H.; Myakalwar, A.K.; Šeborová, P.; Žabka, J.; Abel, B.; Kubelík, P.; Ferus, M. Towards advanced mineral identification for future space mining applications employing LIBS and machine learning. *J. Anal. At. Spectrom.* **2026**, *41*, 615–632. https://doi.org/10.1039/d5ja00377f.
77. Barklem, P.S.; Collet, R. Partition functions and equilibrium constants for diatomic molecules and atoms of astrophysical interest. *Astron. Astrophys.* **2016**, *588*, A96. https://doi.org/10.1051/0004-6361/201526961.
78. Aragón, C.; Aguilera, J.A. Quantitative analysis by laser-induced breakdown spectroscopy based on generalized curves of growth. *Spectrochim. Acta Part B At. Spectrosc.* **2015**, *110*, 124–133. https://doi.org/10.1016/j.sab.2015.06.010.
79. Favre, A.; Bultel, A.; Morel, V.; Lesage, M.; Gosse, L. MERLIN, an adaptative LTE radiative transfer model for any mixture: Validation on Eurofer97 in argon atmosphere. *J. Quant. Spectrosc. Radiat. Transf.* **2025**, *330*, 109222. https://doi.org/10.1016/j.jqsrt.2024.109222.
80. Favre, A.; Abad, A.; Poux, A.; Gosse, L.; Berjaoui, A.; Morel, V.; Bultel, A. Towards real-time calibration-free LIBS supported by machine learning. *Spectrochim. Acta Part B At. Spectrosc.* **2025**, *224*, 107082. https://doi.org/10.1016/j.sab.2024.107082.
81. Gornushkin, I.B.; Völker, T. Intrinsic Performance of Monte Carlo Calibration-Free Algorithm for Laser-Induced Breakdown Spectroscopy. *Sensors* **2022**, *22*, 7149. https://doi.org/10.3390/s22197149.

Disclaimer/Publisher's Note: The statements, opinions and data contained in all publications are solely those of the individual author(s) and contributor(s) and not of MDPI and/or the editor(s). MDPI and/or the editor(s) disclaim responsibility for any injury to people or property resulting from any ideas, methods, instructions or products referred to in the content.